von Karman Institute for Fluid Dynamics

Lecture Series 2025-01

MEASUREMENT, MODELLING AND SIMULATIONS TECHNIQUES FOR NOVEL AIRCRAFT ARCHITECTURES

November 4-6, 2024

MITIGATING ADVERSE AEROACOUSTIC INSTALLATION EFFECTS

M. Azarpeyvand
Department of Aerospace Engineering, University of Bristol, United Kingdo

1 Introduction

Aeroacoustic installation effects refer to the interaction between aerodynamic forces and noise generated by aircraft components during flight. These effects are a critical concern in modern aerospace engineering, as they influence both the operational performance and environmental impact of aircraft. The noise produced by engines, airframes, and other aerodynamic surfaces can contribute significantly to environmental noise pollution, prompting regulatory bodies to impose stringent noise limits. Additionally, installation effects can degrade aerodynamic performance, increasing drag and reducing fuel efficiency. Mitigating these adverse aeroacoustic effects while enhancing the aerodynamic benefits is a key challenge for engineers. A variety of strategies are employed to address this, ranging from innovative design approaches to advanced materials and passive or active noise control technologies. These strategies aim to reduce noise emissions at the source, manage the propagation of sound, and improve the overall aerodynamic efficiency of the aircraft. This lecture will focus on the methods and techniques used to mitigate aeroacoustic installation effects in the ENODISE project, such as flow control devices, porous materials, and optimized design configurations. By understanding the interplay between aerodynamics and acoustics, we can develop more efficient, quieter, and environmentally friendly aircraft.

2 Overview of current noise mitigation techniques

There exist many acoustic mitigation techniques that have been applied to aircraft in order to reduce their environmental impact, however, in the context of the ENODISE project, a selected few technologies and techniques were investigated, in particular with regard to applicability to the boundary layer ingestion configuration. The selected techniques are explored individually with Porous materials covered in Sec. 2.1, Serrated trailing edges in Sec. 2.2, and Acoustic liners in Sec. 2.3. This section will provide a background on these techniques and how they function, with The content covering Porous materials is drawn from Ali et al. (2018b), Ali et al. (2018a), and the content for Serrated trailing edges is drawn from Lyu et al. (2016). The results of applying these techniques to the ENODISE experimental configurations will then be discussed in Sec. 3.

2.1 Porous Materials

In aerospace engineering, the management of aerodynamic noise and enhancement of aerodynamic performance are critical objectives, particularly with growing demands for quieter, more efficient, and environmentally friendly aircraft. Acoustic mitigation techniques, therefore, have emerged as a vital area of study, focusing on methods to reduce the aerodynamic noise generated by aircraft structures without compromising their performance. One promising avenue is the use of porous materials for passive flow control, which has shown significant potential in altering turbulent flows and reducing noise at the source.

Acoustic noise in aerospace applications primarily arises from turbulent flow interactions with aircraft surfaces, such as airfoils, fuselages, and engine components. While effective, traditional noise control methods often involve complex systems that add weight

and complexity to the aircraft design. In contrast, porous materials offer a passive solution by modifying the flow dynamics at a fundamental level. When integrated into trailing edges, airfoils, or other critical surfaces, porous materials have been shown to delay vortex shedding, dampen turbulent fluctuations, and disrupt large-scale coherent flow structures that contribute to noise generation.

Porous treatments function by allowing airflow to penetrate the surface, redistributing the energy in the boundary layer and near-wake regions. This interaction not only reduces pressure fluctuations but also weakens the spanwise coherence of turbulent structures. These modifications lead to a significant reduction in noise, particularly in frequency ranges associated with vortex shedding and other turbulent instabilities. Additionally, the porous medium creates an internal hydrodynamic field that enhances flow stabilization and reduces the energy content of the turbulent boundary layer. Beyond noise reduction, porous materials also offer aerodynamic benefits, such as drag reduction and improved flow stability. By modifying the shape of the boundary layer, porous surfaces can prevent flow separation and reduce aerodynamic losses. This dual advantage of noise reduction and aerodynamic enhancement makes porous treatments an attractive option for aerospace applications, where performance and efficiency are paramount.

The following sections will demonstrate the flow and acoustic characteristics using two experimental setups. We will begin by investigating the flow over a porous surface to establish the fundamental flow mechanics, before then applying porous material to the blunt trailing edge of an aerofoil.

2.1.1 Flow over porous surfaces

This experimental study investigates the interaction between fully turbulent flows and porous surfaces, examining their effects on boundary layer development, surface pressure fluctuations, and noise generation. A flat plate with interchangeable sections—featuring both smooth and porous surfaces with varying porosities and permeabilities—was employed to assess how these surface treatments influence the aerodynamic characteristics. The experimental setup incorporated multiple wall pressure transducers to capture detailed measurements of pressure fluctuations and their coherence along the plate surface. The flow measurements have been performed using a flat plate with a streamwise length of L = 1500 mm, spanwise length of W = 715 mm, and thickness of h = 20 mm. The general layout of the flat plate test-rig is shown in Fig. 1(a). Figure 1(b) provides a schematic of the porous insert installation. An 18 mm wide solid wedge is placed on either sides of the porous insert to avoid any possible flow separation at the porous-solid interface (x = 0 and x = 120 mm). In order to avoid air bleeding through the porous inserts, the bottom part of the porous samples was covered and sealed using a solid medium density fibre (MDF) sheet. Three metal foams with the PPI (pores per inch) of 25, 45, and 80 were used for this study

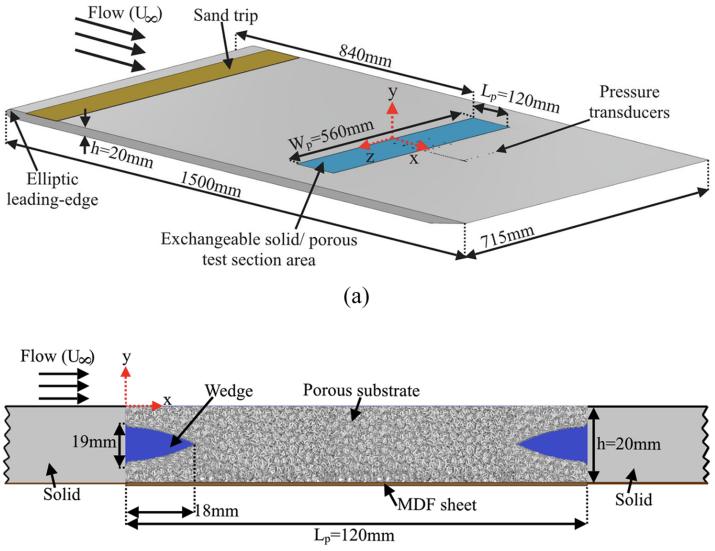


Figure 1: (a) Flat plate experimental setup and (b) illustration of the porous substrate installation.

The 3D images of the porous materials are shown in Fig. 2. The effectiveness of porous treatments for flow and noise control depends primarily on porosity (ϕ) and permeability (κ), both of which were measured for the porous samples in this study. Porosity, defined as the proportion of the material's volume occupied by pores, was determined using a computed tomography scanner, yielding values of 90.92%, 88.39%, 85.37%, and 74.76% for the 25, 35, 45, and 80 PPI samples, respectively. Permeability, which governs fluid penetration, was measured using a test rig with static and total pressure taps. The permeability values were calculated as 8.2×10^{-8} m^2, 4.4×10^{-8} m^2, 2.1×10^{-8} m^2, and 7.7×10^{-9} m^2 for the 25, 35, 45, and 80 PPI samples, respectively. Surface roughness, another key factor, was measured using a non-contact profilometer. The roughness values (R_a) were 1922 μm, 1791 μm, 1761 μm, and 212 μm for the same samples. The relationship between permeability and roughness for these porous materials is shown in Fig. 2.

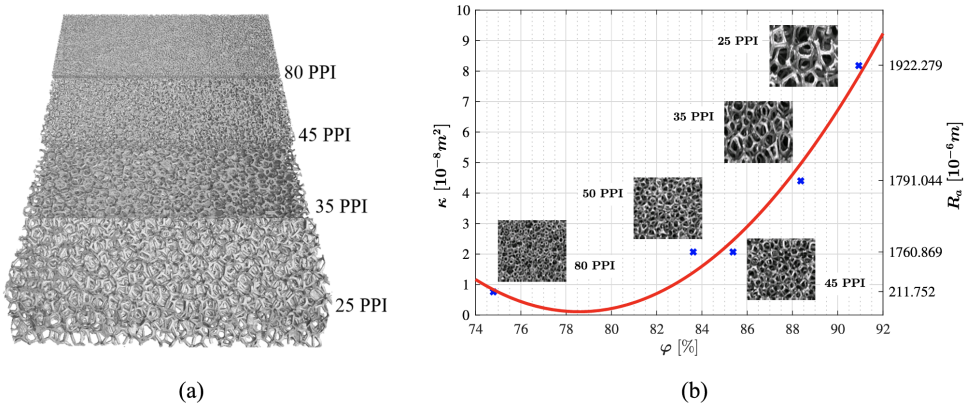


Figure 2: (a) Uncompressed metal foams used in this study and (b) permeability and surface roughness as a function of porosity.

To gain a deeper understanding of the boundary layer flow structures and the influence of porous surfaces, the boundary layer velocity is examined. Figure 3 presents the normalised time-averaged mean and root-mean-square (rms) velocity profiles of the boundary layer at various streamwise locations (BL2–BL7), as indicated in Fig. 4.

The experimental results reveal that less permeable surfaces, such as the 80 PPI and 45 PPI materials, exhibit increases in boundary layer thickness, displacement thickness, and momentum thickness compared to the baseline solid surface. In contrast, the highly permeable 25 PPI surface shows an increase in displacement and momentum thickness relative to the solid case but has lower values than those observed for the 80 PPI and 45 PPI surfaces. Notably, the boundary layer thickness for the 25 PPI surface is the lowest among all cases, likely due to its high permeability, which allows the boundary layer to penetrate deeper into the porous material, effectively reducing the thickness.

Measurements were conducted at a free-stream velocity of $U_\infty = 20\,\mathrm{m/s}$, corresponding to a Reynolds number of $Re_{BL1} = 3.6 \times 10^4$. A single-wire probe was utilized for data collection, achieving fine spatial resolution between $y \approx 0\,\mathrm{mm}$ and $120\,\mathrm{mm}$. Measurements were taken across the entire test section area at $x = 30\,\mathrm{mm}$, $60\,\mathrm{mm}$, and $110\,\mathrm{mm}$, as well as at upstream ($x = -2\,\mathrm{mm}$) and downstream ($x = 130\,\mathrm{mm}$, $205\,\mathrm{mm}$, and $266\,\mathrm{mm}$) locations to provide a comprehensive view of the boundary layer behaviour. The boundary layer profiles were normalised using the thickness measured upstream at $BL1$ (at $x = -2\,\mathrm{mm}$). At this location, the fluid velocity in the x-direction approaches zero due to the no-slip condition at the solid boundary. This behaviour differs from that of the porous boundary, where flow penetration occurs. As expected, the mean velocity profiles at $BL1$ upstream of the test section were similar for all cases and are not presented here. For the solid wall, turbulent boundary layer growth was consistent across all measurement locations, while distinct growth patterns were observed downstream for the porous surfaces, particularly for the 80 PPI and 45 PPI materials. In contrast, the highly permeable 25 PPI surface exhibited different behaviour, likely related to flow penetration effects.

Additionally, the normalised root mean square (rms) of the fluctuating flow velocity clearly shows that the energy cascade within the boundary layer changes significantly due to interactions with the porous surfaces. The rms velocity results for the solid wall indicated lower velocity fluctuations near the wall, which gradually decreased to match the free-stream velocity as the distance increased. In comparison, the porous cases—especially the highly permeable 25 PPI material—revealed drastically different boundary layer behaviour, particularly at measurement locations BL3 ($x/\delta_{BL1} = 2.4$) and BL4 ($x/\delta_{BL1} = 4.4$) over the porous section, and at downstream locations BL5 ($x/\delta_{BL1} = 5.2$), BL6 ($x/\delta_{BL1} = 8.2$), and BL7 ($x/\delta_{BL1} = 10.6$).

Significant increases in rms velocity magnitude and the emergence of peak velocities (at $y/\delta_{BL1} \approx 0.05 - 0.5$) were observed in the near-wall region as the flow travelled over the porous materials (particularly at BL3 and BL4). However, the peaks in rms velocity diminished and flattened downstream of the porous surface (at BL6 and BL7), peaking around $y/\delta_{BL1} \approx 0.5$. It was also noted that the turbulent energy content increased in the normal direction from the wall and subsequently reverted to the standard boundary layer profile (solid surface) at $y/\delta_{BL1} > 1$. This increase in the energy content of the velocity fluctuations near the porous surface led to heightened flow shear stress, attributed to the frictional forces resulting from the rough surface of the material. These findings are consistent with the surface roughness results presented previously.

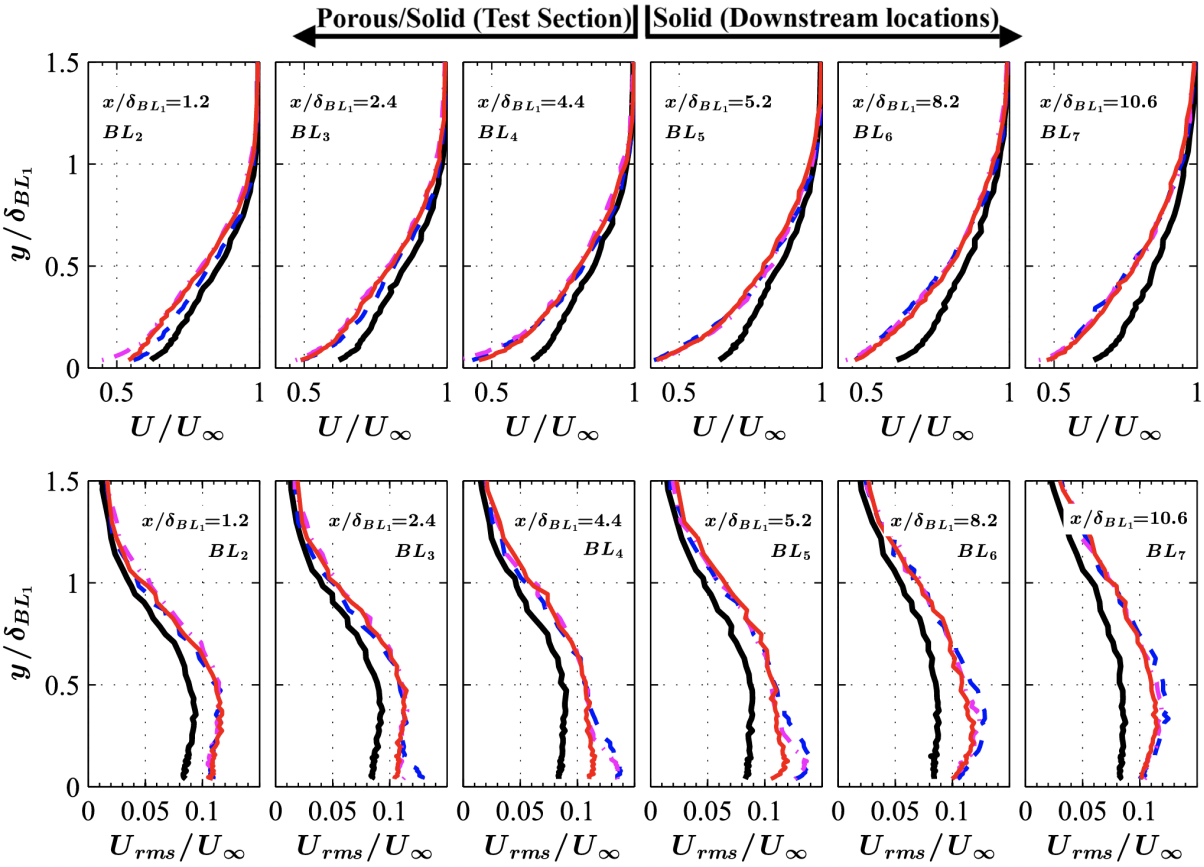


Figure 3: Boundary layer mean and RMS velocity profiles at different streamwise locations over the flat plate. Solid (black solid curve), porous 80 PPI (red solid curve), porous 45 PPI (pink dotted-dashed curve), and porous 25 PPI (blue short-dashed curve).

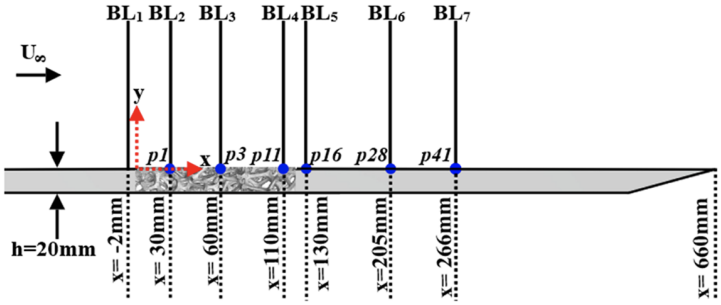


Figure 4: The schematic of the flat plate and the position of the hot-wire for boundary layer (BLI) measurements.

To understand the effects of the porous surface on the boundary layer and the surface pressure fluctuations, a series of unsteady pressure measurements were conducted over and downstream of the porous section. Figure 5 shows the point spectra of the surface pressure fluctuations $\phi_{pp}(f)$, obtained from transducers positioned over the porous section [p_3 ($x/\delta_{BL1} = 2.4$) and p_{11} ($x/\delta_{BL1} = 4.4$)] and downstream [p_{16} ($x/\delta_{BL1} = 5.2$) and p_{41}

$(x/\delta_{BL1} = 10.6)]$. The locations of these transducers are indicated in Fig. 1(a). The measurements indicate that the presence of a porous surface increases the broadband energy content of pressure fluctuations across the entire frequency range for the transducers located over the porous section (p_3 and p_{11}). Notably, a small broadband hump appears between $f = 100$ Hz and 400 Hz at these locations and at p_{16} downstream, particularly for highly permeable samples (25 and 45 PPI). However, this broadband hump dissipates quickly at further downstream locations, such as p_{41}, which is located $5.4\delta_{BL1}$ downstream of the porous section. The observed increase in broadband energy content and the formation of the hump may be attributed to either (a) frictional forces between the rough porous surface and the flow or (b) the presence of a localised strong hydrodynamic field within the porous medium. Additionally, the results show a reduction in fluctuations ϕ_{pp} for high frequencies ($f > 7000$ Hz) at locations downstream of the porous section (p_{41}).

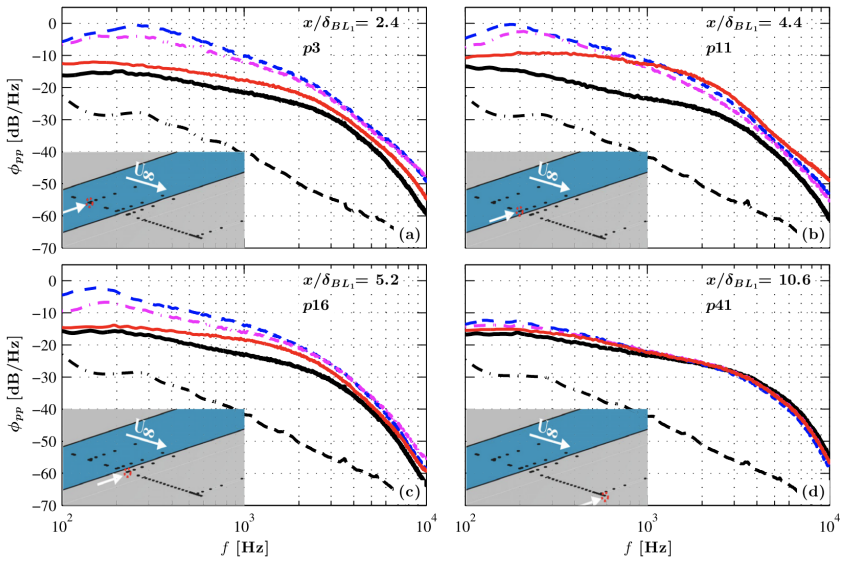


Figure 5: Point spectra of pressure fluctuations at different streamwise locations over and after the porous surface. Solid (black solid curve), porous 80 PPI (red solid curve), porous 45 PPI (pink dotted-dashed curve), porous 25 PPI (blue short-dashed curve), and background noise (black dotted-dashed curve).

2.1.2 Porous trailing edge

In this section, we will provide a comprehensive and systematic investigation of the characteristics and properties of a porous trailing edge. The focus will be on various aspects of flow-porous interactions, including scrubbing effects, the disruption of coherent boundary layer structures, flow penetration, the internal hydrodynamic field, flow discharge, and vortex shedding attenuation. The experimental setup features a flat plate with a blunt trailing edge, which presents complex flow dynamics that can significantly impact aerodynamic and aeroacoustic performance. By analysing the effects of porous treatments applied to the trailing edge, we can see how they can enhance the overall efficiency and noise reduction capabilities of aerodynamic surfaces.

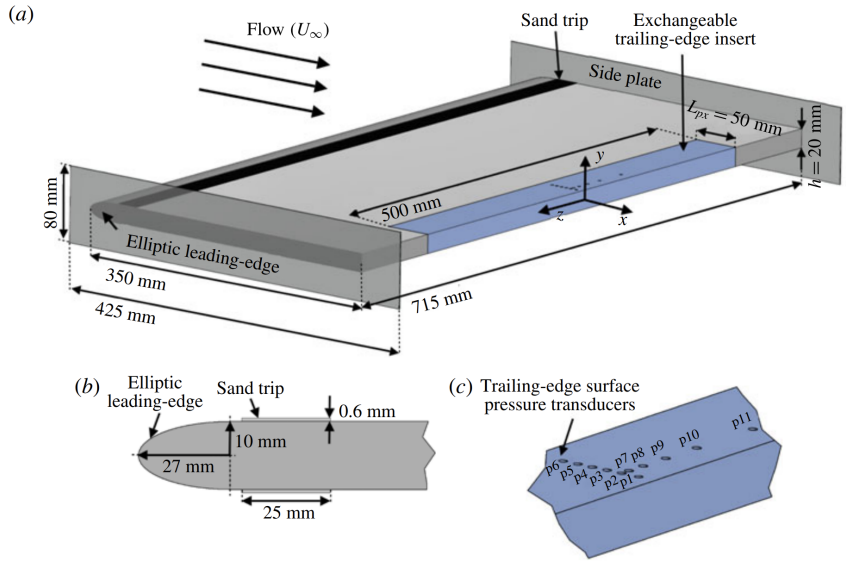


Figure 6: (a) The schematic of a flat plate with an elliptical leading edge and exchangeable blunt trailing edge. (b) The geometry of the elliptic leading edge. (c) The position of the trailing-edge pressure transducer array

To investigate the effects of the porous trailing edge on boundary layer structures, wake development, and vortex shedding, measurements were conducted using Particle Image Velocimetry (PIV) and hot-wire anemometry at a flow velocity of $U_\infty = 20\,\mathrm{m/s}$, corresponding to a Reynolds number of $Re_{Lx} = 4.6 \times 10^5$. Figure 7 presents the time-averaged normalised streamwise (U) and vertical (V) velocity components for the blunt trailing edge, comparing both porous and solid treatments.

We categorise vortex shedding regimes in the wake velocity profile by examining the vortex formation length and the region of vortex cores (mean recirculation). The non-dimensionalised vortex formation length $\left(\frac{L_f}{h}\right)$ is defined as the distance from the trailing edge to the end of the vortex region, where maximum streamwise velocity fluctuations occur. Meanwhile, the non-dimensionalised vortex cores region $\left(\frac{x_{vc}}{h}\right)$ indicates the position of the recirculation core, as illustrated in Figure 7(a). Results show that for the solid trailing edge, flow recirculation occurs within $0.05 < \frac{x}{h} < 1.04$, forming a pair of symmetric counter-rotating vortices near the wake. In contrast, the porous medium with lower permeability (80 PPI) shifts the recirculation region slightly downstream, occurring within $0.15 < \frac{x}{h} < 1.06$, with nearly symmetric vortices but a slight offset between the cores, as shown in Figure 7(c) and 7(d). However, the highly permeable 25 PPI surface significantly alters the vortex core structure and recirculation zone, moving it further downstream to $0.5 < \frac{x}{h} < 1.8$ (Figure 7(e) and 7(f)). The values for $\frac{L_f}{h}$ and $\frac{x_{vc}}{h}$ are 1.04, 1.06, and 1.8, and 0.4, 0.64, and 1.2 for the solid, porous 80 PPI, and porous 25 PPI trailing edges, respectively. This indicates a significant delay in vortex shedding due to flow interactions with the porous treatment, consistent with the drag reduction observed previously. Another interesting feature observed is the area of flow acceleration over the trailing edge, attributed to the pressure difference at this location. This effect relates to the development of the vortex core, which generates a low-pressure region that creates a suction effect, allowing flow acceleration near the trailing edge. The flow acceleration

region for the solid trailing edge can be seen within $-1 < \frac{x}{h} < 0.5$ and $-1.3 < \frac{y}{h} < -0.5$ (Figure 7a), followed by a rapid vertical flow movement and a velocity overshoot leading to flow recirculation in the near-wake region.

In the case of the porous 80 PPI trailing edge, a broader but less intense flow acceleration region is observed compared to the solid case (Figure 7c). However, the porous 25 PPI shows a more streamlined behavior, with reduced flow acceleration upstream of the trailing edge and lower velocity overshoot over the blunt edge. Additionally, the acceleration region for the vertical component V in the wake for the porous 25 PPI moves further downstream than for the solid and 80 PPI cases. These significant changes are believed to result from the penetration of boundary flow into the porous medium, the creation of an internal hydrodynamic field, and the discharge of flow into the wake region.

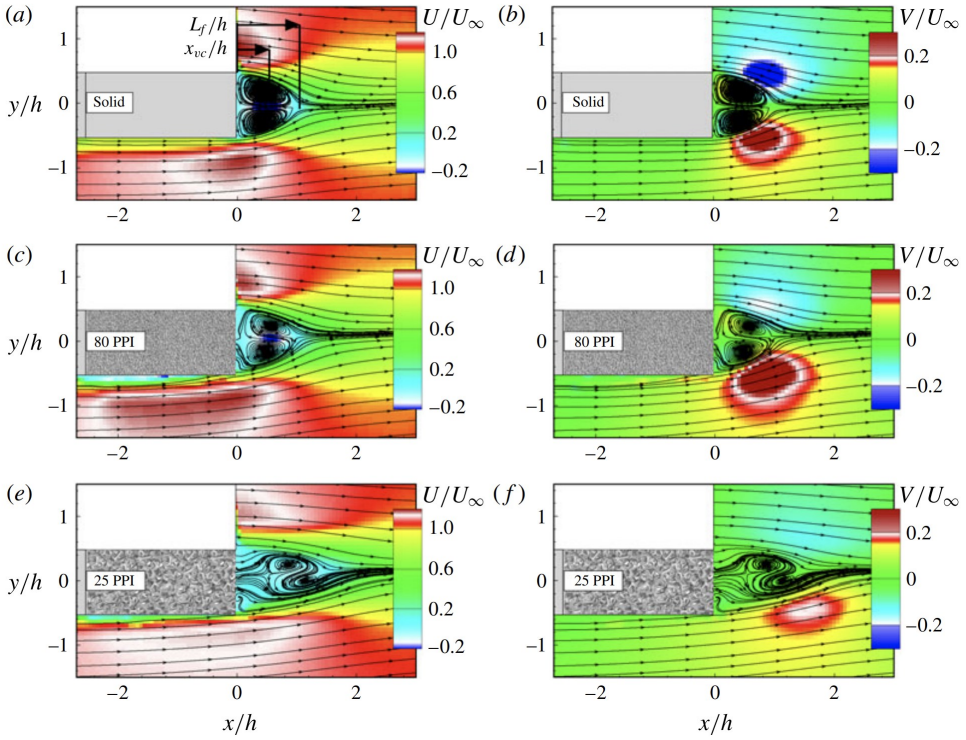


Figure 7: Time-averaged flow pattern for normalized streamwise (U) and vertical (V) velocity components for solid (a,b), porous 80 PPI (c,d) and 25 PPI (e,f).

Figure 8 shows the mean and root-mean-square (r.m.s.) boundary layer velocity profiles along the boundary layer (BL) lines depicted in Figure 5. Measurements were taken at a flow velocity of $U_\infty = 20\,\mathrm{m/s}$ using a single hot-wire probe, collecting data between $y_0/h \approx 0$ and $y_0/h = 2.5$ at 35 stations above the plate, where $y_0 = 0$ is the plate's top surface, as defined in § 2.1.

The distance from the surface (the y_0-axis) is normalised by the boundary layer thickness at $BL1$ ($x/h = -2.6$), located upstream of the trailing-edge section. At $BL1$, the flow velocity approaches zero due to the no-slip condition, which does not apply over the porous surface because of flow penetration. The results indicate an increasing velocity gradient from $BL1$ to $BL4$, suggesting a favourable pressure gradient that enhances flow acceleration over the trailing edge. The velocity profiles for the solid trailing edge deviate

from a standard turbulent boundary layer profile downstream of $BL1$, showing a velocity overshoot at $y_0/\delta_{BL1} = 1$, which remains relatively constant with x/h. The r.m.s. velocity measurements indicate that the solid trailing edge exhibits higher fluctuations than the porous cases across most of the boundary layer. For the 80 PPI trailing edge, the profiles resemble those of the solid trailing edge but with a milder overshoot. The porous 80 PPI treatment reduces r.m.s. velocity across a significant part of the boundary layer. In contrast, the porous 25 PPI treatment leads to a more streamlined flow with less acceleration and reduced velocity overshoot. The r.m.s. velocity shows abrupt changes in the outer regions at $x/h = -0.9$ (BL3) and $x/h = -0.05$ (BL4). Near the wall, the porous 25 PPI exhibits increased r.m.s. velocity despite overall reductions in U_{rms}. This increase is attributed to frictional forces at the porous surface. Notably, the 25 PPI treatment enhances the energy content of the velocity fluctuations near the porous surface, indicating that porous treatments can effectively reduce the energy of large coherent structures responsible for low-frequency pressure fluctuations and trailing-edge noise generation.

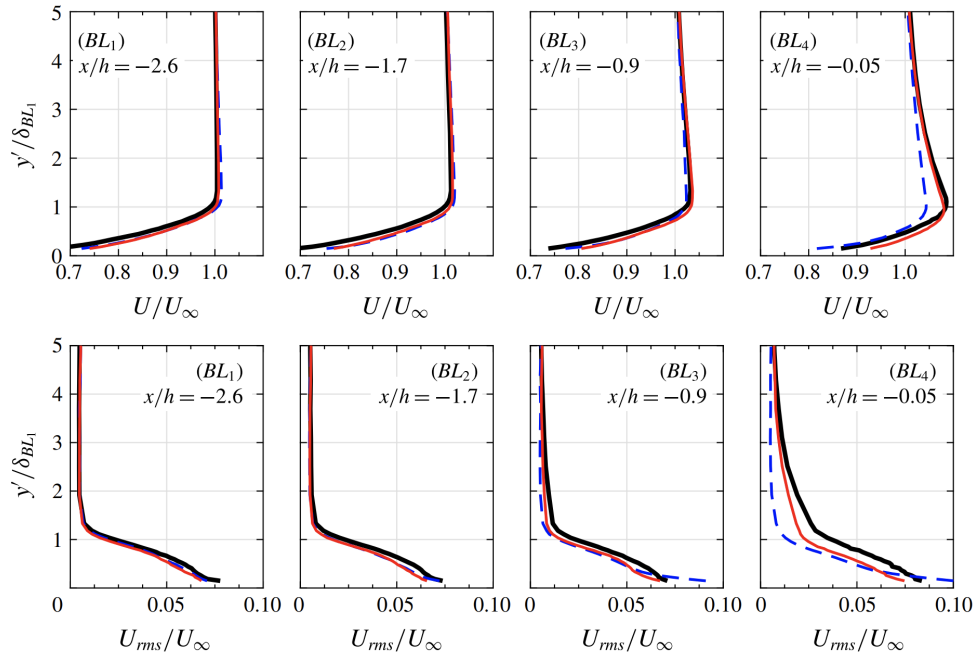


Figure 8: Boundary layer mean and r.m.s. velocity profiles at different streamwise locations upstream of the trailing edge. Solid trailing edge (——), porous 80 PPI trailing edge (——), porous 25 PPI trailing edge (- - -).

Figure 9 illustrates the streamwise (U) and vertical (V) velocity profiles at various axial locations downstream of the trailing edge, specifically at $x/h = 0.1, 0.5, 1.0, 2.0, 3.0$, and 5.0. Hot-wire anemometry was used for these measurements, so the streamwise velocity is always presented as a positive value. The results indicate that porous treatments significantly alter flow structures in the near-wake region, notably reducing the streamwise velocity magnitude. Specifically, the porous cases delay vortex shedding, demonstrating near-wake stabilisation, which aligns with the streamlined flow patterns observed earlier. The 25 PPI treatment shows a large velocity deficit due to suppressed recirculation and reduced velocity overshoot, resulting in a more streamlined flow and greater deficits in

the near-wake region. This porous material limits the entrainment of high-momentum fluid from the free stream, leading to lower momentum transfer in the wake and larger velocity deficits. Moreover, the reduced impact of vortex shedding enhances base pressure recovery, contributing to a decrease in drag coefficient (C_D). The drag associated with vortex shedding can be calculated using the wake velocity deficit method:

$$C_{D_W} = \frac{2}{A}\int \frac{U}{U_\infty}\left(1 - \frac{U}{U_\infty}\right) dy + \frac{2}{A}\int \left(\frac{U_{rms}}{U_\infty}\right)^2 dy,$$

where A is the plate area and the integrals are evaluated outside the vortex recirculation region in the near-wake. The calculations for the current study are based on data at $x/h = 2$. At a flow velocity of $U_\infty = 20\,\mathrm{m/s}$ (Reynolds number $Re_{Lx} = 4.6 \times 10^5$), the results show a significant reduction of approximately 15% in total drag (C_{D_W}) for the 25 PPI trailing edge compared to the solid case. The vertical velocity component (V) displays different behaviour compared to the streamwise component. In the near-wake, the V component correlates with vortex formation and roll-up. The solid trailing edge at $x/h = 0.1$ shows a small secondary recirculation near the centerline, which quickly dissipates downstream, leaving one large recirculation area by $x/h = 2.0$ to 3.0. The V profiles for the 80 PPI trailing edge resemble those of the solid edge, while the 25 PPI trailing edge exhibits a much weaker main recirculation area, indicating stabilised shear layers and delayed vortex shedding formation.

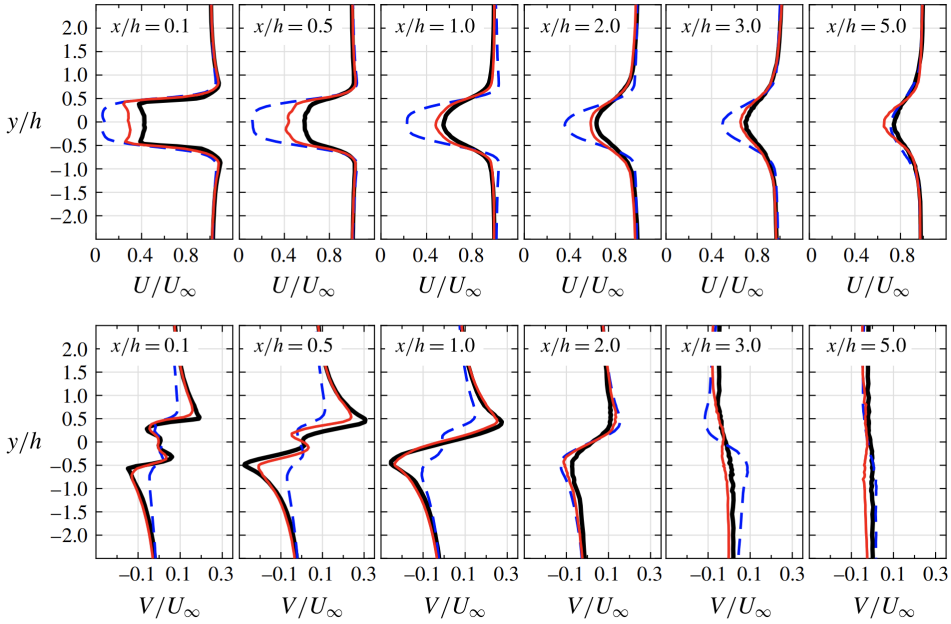


Figure 9: Mean streamwise (U) and vertical (V) velocity components in the wake of the blunt trailing edge. Solid trailing edge (——), porous 80 PPI trailing edge (——), porous 25 PPI trailing edge (- - -).

Figure 10 presents the power spectral density (PSD) of wake flow velocity (ϕ_{uu}) at various downstream locations along the lip line ($y/h = 0.5$) and centerline ($y/h = 0$), downstream of the trailing edge. The measurements reveal distinct vortex shedding frequencies, including the fundamental and harmonic frequencies, for the solid trailing edge.

The velocity spectra show a slope near $f^{-5/3}$ after the second harmonic ($St = 0.6$), consistent across all locations. For the porous cases, significant reductions in broadband energy content are observed. The 80 PPI porous treatment, while reducing broadband energy, does not suppress the tonal peaks, making the vortex shedding tones more pronounced relative to the solid case. In contrast, the 25 PPI treatment effectively suppresses both the vortex shedding peaks and the broadband content of velocity fluctuations, particularly in the near-wake region. A broadband hump between $0.3 < St < 1.0$ is visible for the 25 PPI case, local to the trailing edge and dissipating further downstream, likely due to the internal hydrodynamic field within the porous material. Additionally, the 25 PPI porous treatment leads to a significant reduction in the energy content of wake structures in the near-wake, with some energy recovery at $x/h = 2.0$, followed by a further reduction in both peak and broadband energy in the far-wake region ($x/h = 5.0$).

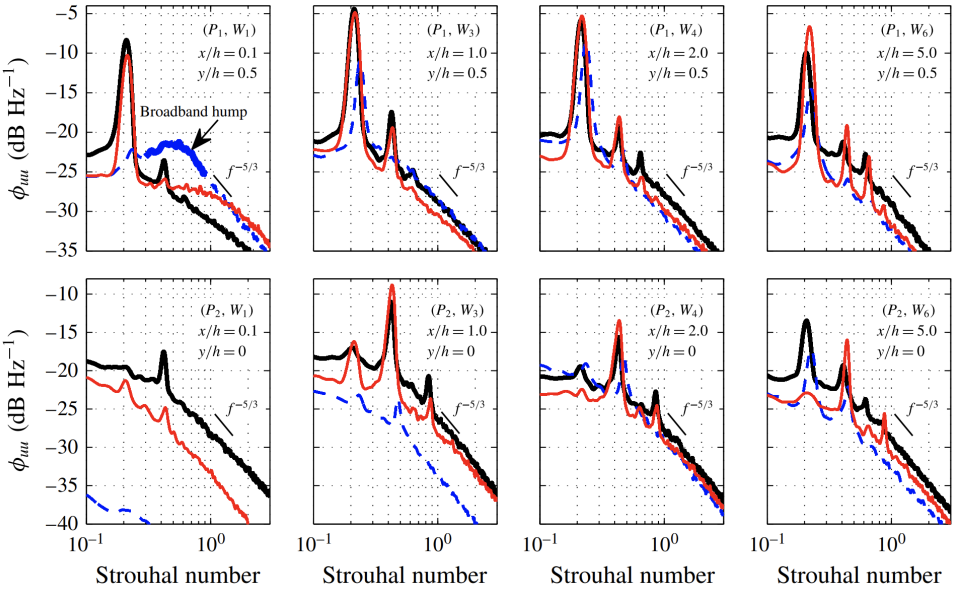


Figure 10: Mean streamwise (U) and vertical (V) velocity components in the wake of the blunt trailing edge. Solid trailing edge (——), porous 80 PPI trailing edge (——), porous 25 PPI trailing edge (- - -).

Finally, the acoustic effects of the porous trailing edge is examined. The sound pressure level (SPL) as a function of the Strouhal number ($\mathrm{St} = \frac{fh}{U_\infty}$) for far-field microphones positioned at polar angles of 45°, 60°, 90°, and 120°, with a flow velocity of $U_\infty = 30\,\mathrm{m/s}$, is shown in Fig. 11. The SPL spectrum is calculated using:

$$\mathrm{SPL} = 20 \cdot \log_{10}\left(\frac{P_{\mathrm{rms}}}{P_{\mathrm{ref}}}\right)$$

where P_{rms} is the root-mean-square of the acoustic pressure, and $P_{\mathrm{ref}} = 20\,\mu\mathrm{Pa}$ is the reference pressure. The energy content at different frequencies was estimated using Welch's power spectral density method, applied to the time-domain pressure data with a Hamming window and 50% overlap, yielding a frequency resolution of 32 Hz. The power spectrum was corrected to a reference distance of 1 meter. The noise from the plate was well above the background noise across all frequencies of interest. The results reveal a

tonal peak at St ≈ 0.2 for the solid trailing edge, corresponding to the fundamental vortex shedding frequency. Additionally, a double peak near this frequency emerges, indicating two distinct vortical structures in the wake. For the porous 80 PPI treatment, a consistent reduction in vortex shedding tonal peaks is observed across all angles. In the 25 PPI case, no tonal peak is detected, confirming that vortex shedding has been effectively eliminated. The tonal peak for the solid trailing edge is about 25 dB above the broadband energy, while for the 80 PPI it is reduced to approximately 18 dB, and it is nearly negligible for the 25 PPI case at all polar angles.

However, the 25 PPI treatment results in an increase of broadband noise levels in the high-frequency range by 8–10 dB, likely due to friction between the flow and the rough porous surface. An interesting observation for the solid trailing-edge case is the appearance of a double peak, with a dominant peak at St ≈ 0.2 and a secondary peak at St ≈ 0.18, which is less prominent at certain angles. This could be attributed to spanwise variations in vortex shedding, with the dominant peak corresponding to regular shedding behind the trailing edge, and the secondary peak associated with lower-frequency shedding near the edge.

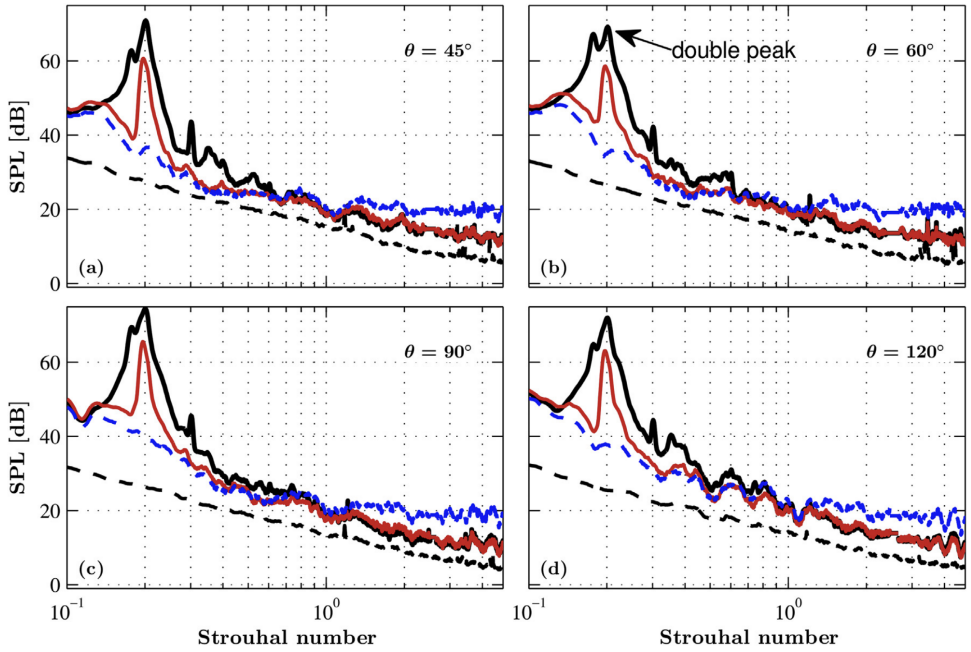


Figure 11: Sound pressure level spectra of the far-field pressure fluctuations with reference to 20 μ Pa at polar angles of θ = 45o, 60o, 90o and 120o, measured at U_∞ = 30 m/s. Solid trailing edge (black), Porous 80 PPI trailing edge (red), Porous 25 PPI trailing edge (blue), Background noise (black-dashed).

The directivity plots at different frequencies for flow speed $U_\infty = 30\,\mathrm{m/s}$, with and without porous treatments, are shown in Fig. 12. The results are scaled differently to improve clarity and visualisation. At St = 0.1, the amplitude of the acoustic waves remains nearly unchanged for all cases, indicating that the porous treatment has minimal effect on far-field microphone directivity at this frequency. However, at St = 0.2, the directivity peaks at $\theta = 90°$ with the lowest directivity observed at the downstream location ($\theta = 25°$) for all trailing edge configurations. The amplitude of the vortex

shedding tone at St = 0.2 is reduced for the porous treatments, with the 25 PPI case showing a reduction of up to 35 dB at $\theta = 90°$. As the frequency increases (St = 0.3 and St = 0.4), the sound directivity pattern shows more lobes, and the noise reduction effect from the porous treatments diminishes across all angles. At higher Strouhal numbers (St = 1.0, 1.5, 2.0), the 25 PPI case exhibits a noise increase, which may be attributed to the roughness of the porous surface. This observation aligns with the surface roughness measurements discussed earlier. In contrast, the directivity of the 80 PPI porous material remains similar to that of the solid case at high frequencies, as its lower roughness value (R_a) likely contributes to less noise generation.

The overall sound pressure level (OASPL) is calculated by integrating the energy spectrum over the frequency range from 100 Hz to 32 kHz. Fig. 12 shows the directivity of the OASPL for the solid and porous trailing edges at different flow speeds (U_∞ = 20 m/s, 30 m/s, 40 m/s, 50 m/s). The porous treatments reduce the overall sound pressure levels across all polar angles, with the 25 PPI material showing the most significant reduction. As flow speed increases, the OASPL increases for all cases, but the reduction due to the porous treatments becomes less pronounced, particularly at higher velocities ($U_\infty > 30$ m/s). Notably, the difference in noise reduction between the 80 PPI and 25 PPI materials becomes minimal at higher speeds. In the downstream direction ($\theta \leq 45°$), the porous treatments offer much smaller noise reductions at all velocities.

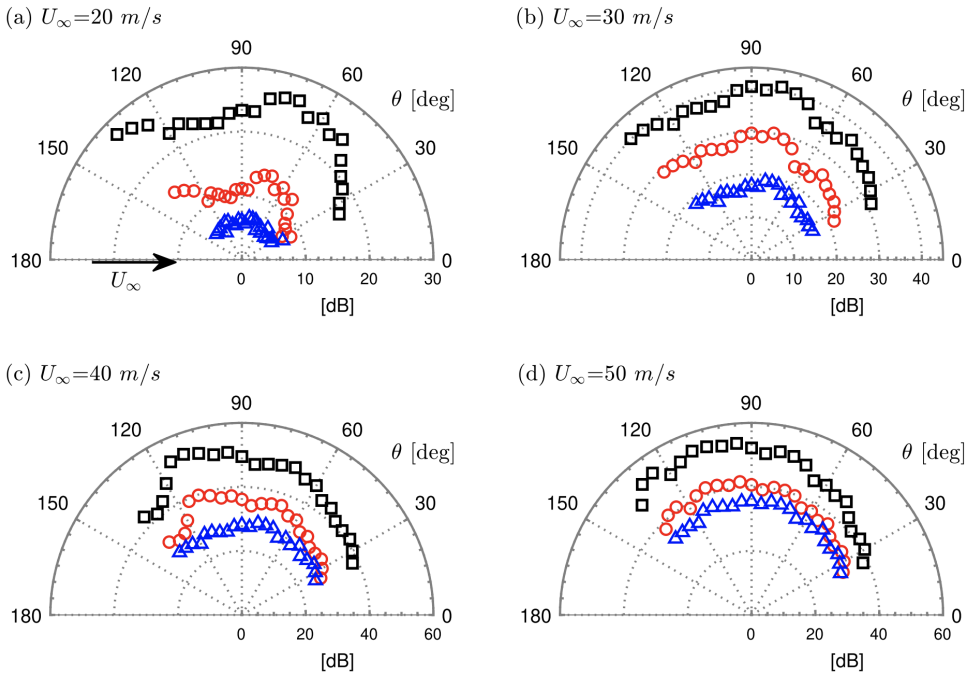


Figure 12: Overall sound pressure level (OASPL) of the acoustic waves generated by the trailing edge configurations with and without the porous treatments at U_∞ = 20 m/s,30 m/s, 40 m/s and 50 m/s. Solid trailing edge (□), Porous 80 PPI trailing edge (○) and Porous 25 PPI trailing edge (△).

2.2 Serrated Trailing Edge

This section will discuss the characteristics of a serrated trailing edge, and its effect on the flow and resulting far-field noise. In the field of aeroacoustics, trailing-edge noise generated by airfoils during turbulent boundary layer interactions is a major contributor to overall aerodynamic noise. This is a critical issue in industries such as aviation and wind energy, where noise control has become increasingly important due to stricter regulations and growing environmental concerns. One of the most effective passive noise mitigation techniques is the application of serrated trailing edges, which alter the flow structure to reduce noise radiated by turbulent eddies. Trailing-edge serrations typically take the form of sawtooth or sinusoidal patterns applied to the edge of an airfoil. These serrations work by disrupting the coherence of turbulent eddies—the primary source of noise in trailing-edge scenarios. As the serrations scatter pressure waves from the turbulent boundary layer, they diminish the intensity of the noise radiated into the far field. Studies and models, such as those developed by Howe, demonstrate that serrations can lead to substantial noise reductions, often up to 10 dB, under certain flow conditions. The degree of effectiveness depends heavily on the geometry of the serrations and the specific aerodynamic environment.

Serrated edges are particularly efficient in reducing noise at lower frequencies and can alter the directivity of noise radiation by inducing destructive interference in sound waves scattered at the trailing edge. However, at higher frequencies or Mach numbers, the benefits of noise reduction can lessen, and in some cases, serrations may even increase noise. Research has shown that the effectiveness of serrations depends on key geometric factors, including their sharpness, amplitude (height), and wavelength. Optimising these parameters for a specific aerodynamic application is essential to achieve meaningful noise reductions without compromising aerodynamic performance. Recent advancements in mathematical models have improved the understanding of how serrations reduce noise and provided deeper insights into their optimal design for various practical applications. We will now go more in-depth into the results of modelling serrated trailing edges. An

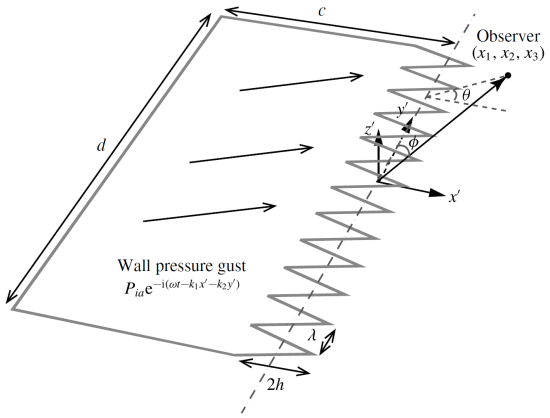


Figure 13: The schematic of a flat plate with trailing-edge serrations.

aerofoil with trailing-edge serrations can be modelled as a flat plate with infinitesimal thickness, an average chord length c, and a spanwise length d. The coordinates x_0, y_0, and z_0 represent the streamwise, spanwise, and normal directions relative to the plate.

The position of the observer is denoted by (x_1, x_2, x_3). The shape of the serrated edge is described by a profile function $H(y_0)$, which oscillates with zero mean and equals zero when no serrations are present. As illustrated in figure 13, a typical sawtooth serration has a root-to-tip amplitude of $2h$ and a wavelength λ.

The normalised sound power spectra for different serration configurations at $M_0 = 0.1$ are shown in figure 14 (a–f). The spectrum for a serrated trailing edge with a sharpness ratio of $4h/\lambda = 0.5$ is displayed in figure 14(a). As expected, the sound reduction remains close to zero across the entire frequency range. Increasing the sharpness of the serrations progressively improves sound reduction, as seen in figures 14(b–d). For sufficiently sharp serrations, significant noise reduction occurs across a broad frequency range, as illustrated in figure 14(e), where the sharpness factor is $4h/\lambda = 10$. The results for a sawtooth serration with $\lambda/h = 0.2$ and $h/c = 0.05$ at $M_0 = 0.1$ are shown in figure 14(f). Comparing figures 14(e) and 14(f), it becomes clear that increasing the sharpness further enhances high-frequency noise reduction, while the performance at low frequencies ($kc < 10$) remains constant. In figure 14(f), the far-field sound reduction is approximately 10 dB at high frequencies, aligning well with experimental results that report reductions of 7–10 dB (Dassen et al., 1996; Parchen et al., 1999). From figures 14(a) and 14(b), it can be observed that a slight noise increase may occur at low frequencies. This effect becomes more pronounced at low frequencies when the Mach number is higher, such as $M_0 = 0.2$.

Figures 15 and 16 display the non-dimensional far-field directivity. The results are presented for both straight and serrated trailing edges with $\lambda/h = 0.4$ at Mach numbers $M_0 = 0.1$ and $M_0 = 0.4$, respectively. As expected, the serrations have little impact on noise generation at very low frequencies ($kc \leq 1$). However, the data show that serrations significantly reduce noise at higher frequencies. This noise reduction is primarily attributed to destructive interference caused by scattering, as discussed earlier. While most experimental studies, such as those by Gruber et al. (2013), focus on noise reduction at small radiation angles and 90° above the trailing edge, figures 15 and 16 demonstrate that serrations are more effective in reducing noise at larger radiation angles, specifically towards the leading edge ($\phi > 90°$). This is an intriguing finding, as noise measurements in laboratory settings are often restricted to angles between 30° and 120° due to limitations such as the size of the anechoic chamber or reflections from the contraction nozzle (Gruber, 2012; Moreau & Doolan, 2013). Additionally, the results indicate that serrations cause significant changes in the directivity pattern of the scattered pressure field at high frequencies. For straight trailing edges, one typically observes a cardioid directivity pattern at high frequencies, consistent with the edge scattering of a half-plane (Williams & Hall, 1970).

In contrast, serrated trailing edges exhibit a more dipolar directivity pattern, with a clear peak at a specific angle that depends on both the serration sharpness and the Mach number. Numerical studies of the directivity for various serration configurations show that as the sharpness of the serrations increases, the expected cardioid shape gradually transitions into a more dipolar pattern, with the directivity peak shifting downstream towards the trailing edge. The dipolar behaviour of noise from serrated trailing edges means that the region near the leading edge ($\phi = 180°$) experiences significantly less noise compared to a straight trailing edge. Increasing the Mach number further shifts the directivity peak toward the trailing edge, as seen by comparing figures 15 and 16. It is also important to note that at higher Mach numbers, as shown in figure 16, serrations

can cause a noticeable increase in noise levels in the trailing-edge region ($0° < \phi < 90°$) for intermediate frequencies ($1 < kc < 10$).

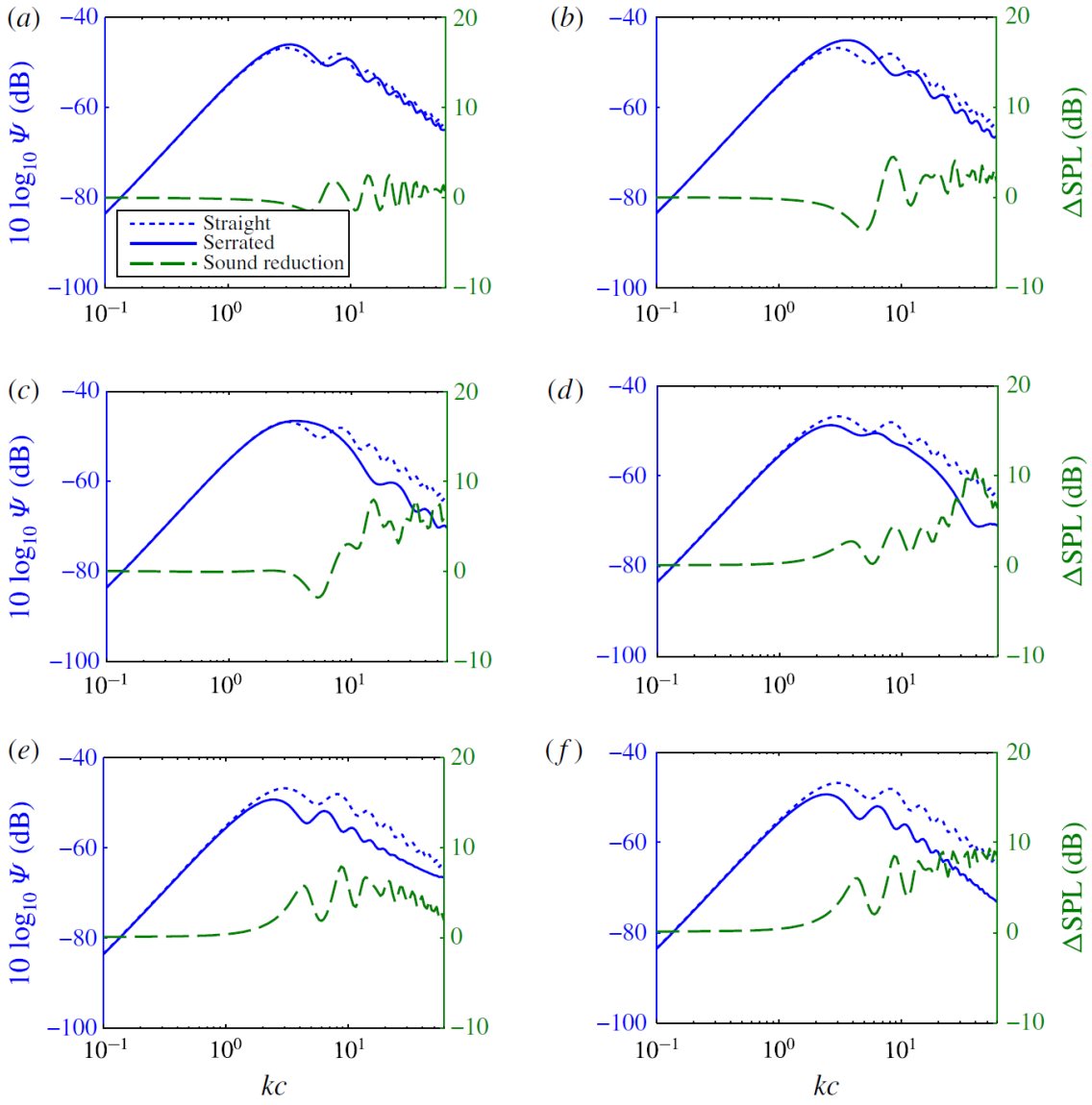


Figure 14: The normalized spectrum (left axis) for serrated and straight trailing edges is shown with solid and dotted blue lines, respectively. The sound reduction spectrum ΔSPL (right axis, green dashed line) is plotted for an observer at $\phi = 90°$ and $x_3/c = 1$, located above the plate in the mid-span plane, with $M_0 = 0.1$. The cases are as follows: (a) $\lambda/h = 8$, $h/c = 0.025$; (b) $\lambda/h = 4$, $h/c = 0.025$; (c) $\lambda/h = 2$, $h/c = 0.05$; (d) $\lambda/h = 1$, $h/c = 0.005$; (e) $\lambda/h = 0.4$, $h/c = 0.05$; (f) $\lambda/h = 0.2$, $h/c = 0.05$.

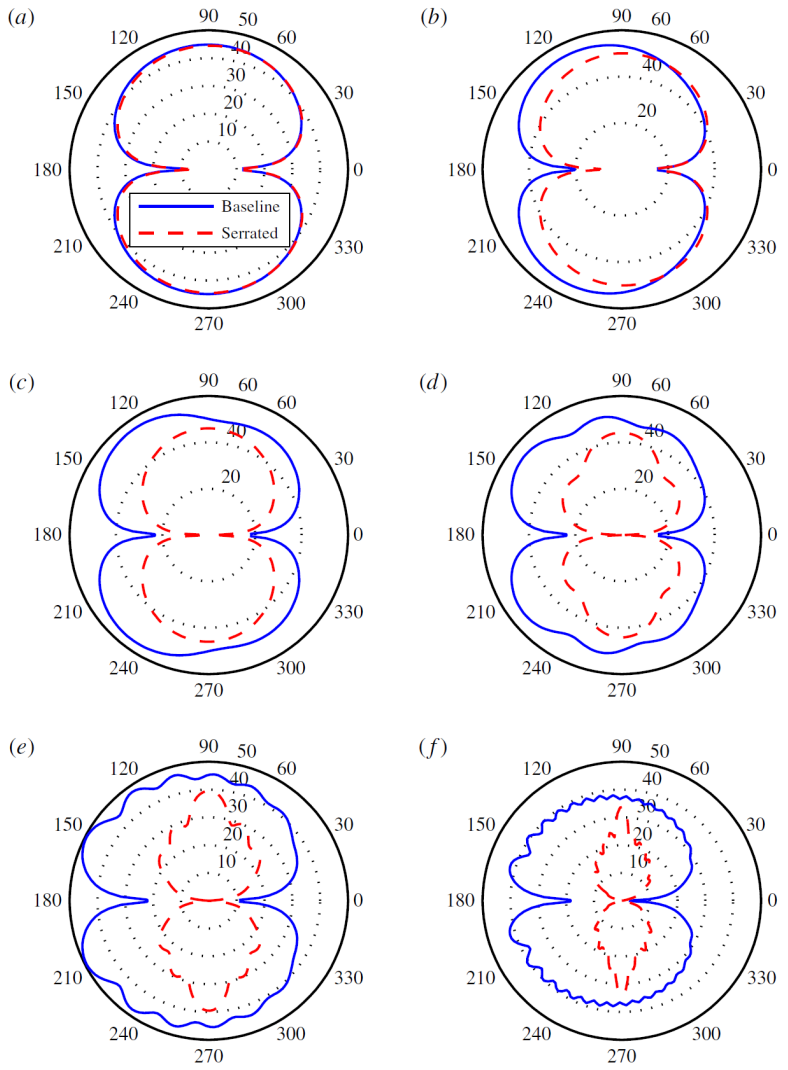


Figure 15: Directivity patterns plotted against ϕ in the mid-span plane ($x_2 = 0$ and $\sqrt{x_1^2 + x_3^2}/c = 1$) at $M_0 = 0.1$ for serrations with $\lambda/h = 0.4$ and $h/c = 0.05$. The far-field sound levels are expressed as $10 \log_{10}(p(x, \omega)/(4 \times 10^{-10}))$. The cases shown are: (a) $kc = 1$, (b) $kc = 3$, (c) $kc = 5$, (d) $kc = 10$, (e) $kc = 20$, and (f) $kc = 50$.

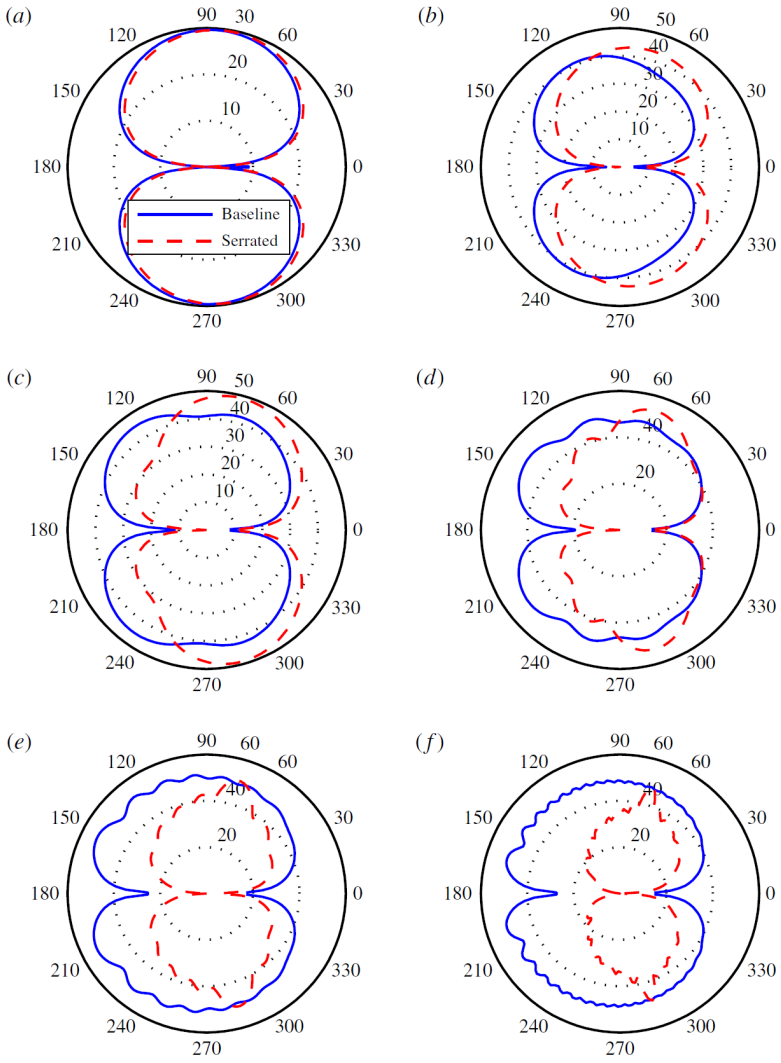


Figure 16: Directivity patterns plotted against ϕ in the mid-span plane ($x_2 = 0$ and $\sqrt{x_1^2 + x_3^2}/c = 1$) at $M_0 = 0.4$ for serrations with $\lambda/h = 0.4$ and $h/c = 0.05$. The far-field sound levels are expressed as $10\log_{10}\left(\frac{p(x,\omega)}{4\times10^{-10}}\right)$. The cases presented are: (a) $kc = 1$, (b) $kc = 3$, (c) $kc = 5$, (d) $kc = 10$, (e) $kc = 20$, and (f) $kc = 50$.

To gain a deeper understanding of the noise reduction mechanism, the pressure distribution across the surface of the flat plate is presented in figures 17–18. The incident pressure consistently raises the far-field sound level by 6 dB; therefore, it is sufficient to focus solely on the scattered pressure distribution. The scattered pressure represents the pressure jump across the flat plate. Two non-dimensional parameters, $k_1 h$ and $k_1 h_e$, are critical for effective sound reduction using serrated trailing edges. The scattered pressure distribution will be illustrated by fixing one parameter while varying the other. The scattered pressure described here arises from wall pressure gusts with $k_2 = 0$, although the analysis also applies to gusts with $k_2 \neq 0$, as the streamwise wavenumber k_1 remains constant across different gusts. Figure 17 presents the scattered pressure distribution on the flat plate for varying values of $k_1 h$. The scattered surface pressure is derived from the real part of equation (2.39) using the second-order approximation (with $P_i = 1$), and

is then normalized to unity. The results shown in figure 17 are for $k_1 h_e = 7$, while $k_1 h$ varies from 2 to 20. The spanwise coordinate y_0 is normalized by the spanwise correlation length l_{y_0}, and the streamwise coordinate x_0 is normalized by the hydrodynamic wavelength $\lambda_1 = \frac{2\pi}{k_1}$. Thus, the distance between adjacent streamwise dashed lines corresponds to the spanwise correlation length l_{y_0}.

In figure 17(a), the scattered surface pressure distribution near the trailing edge is shown for $k_1 h = 2$. The distribution indicates that the scattered surface pressure field between adjacent streamwise lines is essentially in phase, suggesting minimal phase variation within l_{y_0}. Figure 17(b) illustrates the scattered surface pressure distribution for $k_1 h = 4$, where small phase differences start to emerge within the spanwise correlation length. In figure 17(c), for $k_1 h = 10$, a pronounced phase difference is evident within adjacent streamwise lines, even as the spanwise correlation length decreases. Finally, figure 17(d) shows the distribution for $k_1 h = 20$, where the spanwise correlation length further diminishes, yet sufficient phase differences persist within the increasingly narrow ranges.

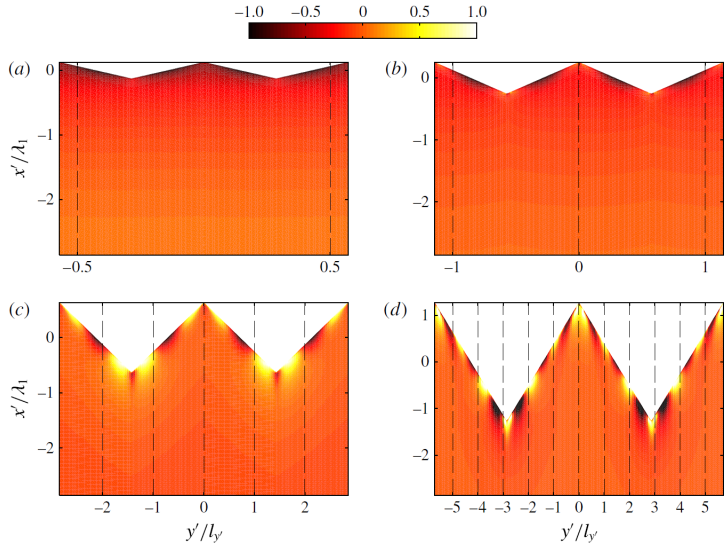


Figure 17: The scattered surface pressure distribution at a fixed frequency for $k_1 h_e = 7$. The cases shown are: (a) $k_1 h = 2$, (b) $k_1 h = 4$, (c) $k_1 h = 10$, and (d) $k_1 h = 20$. The horizontal axis represents the spanwise coordinate normalized by the spanwise correlation length, and the vertical axis represents the streamwise coordinate normalized by the hydrodynamic wavelength.

The scattered pressure distributions for different values of $k_1 h_e$ are shown in figure 18. Here, $k_1 h$ is fixed at 10, while $k_1 h_e$ increases from 1 to 10, as depicted in figures 18(a)–(d). Both the spanwise and streamwise coordinates are normalized by l_{y_0} and λ_1, respectively. Figure 18(a) presents the scattered surface pressure distribution for $k_1 h_e = 1$. Since $k_1 h_e$ is small, the distance between two adjacent dashed lines is much smaller than the serration wavelength. Consequently, although pronounced phase differences appear along the edge, minimal phase variation is observed within a spanwise correlation length. The pressure distribution for $k_1 h_e = 2$ is shown in figure 18(b), and no significant phase variations are observed. However, for $k_1 h_e = 4$, a clear phase variation in the scattered pressure begins to appear between adjacent lines, as shown in figure 18(c). In figure 18(d), where

$k_1 h_e = 10$, pronounced phase differences appear within a correlation length l_{y0} in the spanwise direction.

Now, we can discuss the noise reduction mechanism by examining the physical implications of the two parameters $k_1 h$ and $k_1 h_e$. From figure 17, it is evident that the criterion $k_1 h \gg 1$ ensures effective phase variations along and near the trailing edge in the spanwise direction. Additionally, as shown in figure 18, the condition $k_1 h_e \gg 1$ ensures that phase differences occur within one spanwise correlation length, i.e., between two adjacent dashed lines in figures 17 and 18. Since the surface pressure within the regions bordered by dashed lines remains coherent, and the phase difference occurs over a range much smaller than the acoustic wavelength, far-field sound is reduced due to destructive interference. This indicates that the phase differences induced on the flat plate by serrations should be well-contained within a correlated turbulent structure to achieve sound reduction. As demonstrated in both figures 17 and 18, the noise reduction is due to the destructive interference of the scattered surface pressure caused by the serrations. From the preceding analysis, one can conclude that the minimum effective serration length required for noise reduction is $h_{\min} = \min(h, h_e)$. The two conditions can be combined into one: $k_1 h_{\min} \gg 1$. Therefore, to achieve effective noise reduction in the far field, the serration geometry must satisfy $k_1 h_{\min} \gg 1$. Based on the interference results from figures 17 and 18, a general rule of thumb is $k_1 h_{\min} \gtrsim \pi$, with larger values being more favourable for noise reduction.

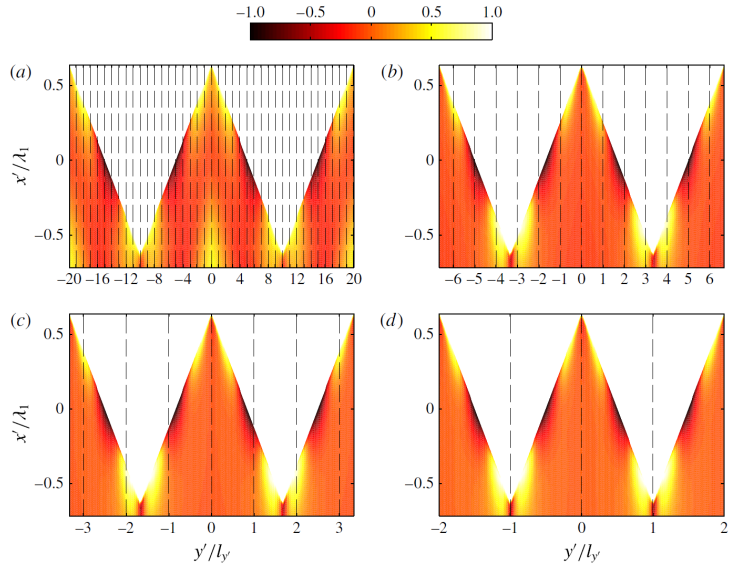


Figure 18: The scattered surface pressure distribution for different serrations at a fixed frequency and $k_1 h = 10$. The cases shown are: (a) $k_1 h_e = 1$, (b) $k_1 h_e = 3$, (c) $k_1 h_e = 6$, and (d) $k_1 h_e = 10$. The horizontal axis represents the spanwise coordinate normalized by the spanwise correlation length, and the vertical axis represents the streamwise coordinate normalized by the hydrodynamic wavelength.

2.3 Acoustic Liners

Acoustic liners are specialized materials and structures used in the aerospace industry to reduce noise, particularly in jet engines and other propulsion systems. Their primary function is to absorb sound waves, minimizing the propagation of the propulsion noise to

the far field. That is critical in reducing environmental noise pollution and the discomfort caused by aircraft noise, particularly during take-off and landing Lilley (2004).

Acoustic liners are primarily used in jet engines to reduce noise from high-speed airflow and engine components Jones et al. (2022), helping to meet strict regulations from authorities. They are also necessary in rotorcraft, especially for Urban Air Mobility (UAM) designs Galles et al. (2022), where minimizing rotor noise is essential in urban environments. Beyond aviation, acoustic liners are used in industrial settings, such as power plants, to control machinery noise and protect workers' hearing. One of the main challenges in designing acoustic liners is balancing noise reduction with aerodynamic efficiency Howerton and Jones (2018). Adding liners to the propulsive system can sometimes change the engine's drag or weight characteristics, which can reduce fuel efficiency. Advanced materials and designs, such as meta-materials or adaptive liners Ma and Su (2020); Ma et al. (2024) that can change acoustic properties in flight are being researched to address these limitations.

Acoustic liners play a critical role in modern aerospace. They ensure that the industry can grow while mitigating noise pollution's environmental and social impacts. The current advancements in material science and design aim to improve the effectiveness and efficiency of acoustic liners, helping the development of quieter, more sustainable aircraft for the future.

2.3.1 Working principle of acoustic liners

Acoustic liners operate on the principle of sound absorption Bauer (1977); Sirotto et al. (2024). These liners consist of a perforated face sheet (which allows sound waves to enter) and a honeycomb core backed by a solid layer, forming a Helmholtz resonator Tang and Sirignano (1973). It consists of a cavity (or chamber) connected to the outside environment by a narrow neck or opening. When sound waves of a particular frequency enter the resonator, they cause the air inside the neck to oscillate while the air in the cavity compresses and expands, dissipating the sound energy as heat and reducing the overall noise level. The resonator's natural frequency f_0 is dependent on the geometry of the neck and cavity and can be approximated by

$$f_0 = \frac{c}{2\pi}\sqrt{\frac{A}{VL}} \tag{1}$$

where A is the cross-section area of the neck, V is the cavity volume, and L is the length of the neck.

In acoustic liners, Helmholtz resonators are often incorporated to target specific noise frequencies, enhancing their ability to absorb sound in a controlled manner. The configuration where a perforated plate is placed over a honeycomb liner is called a *Single Degree of Freedom* (SDOF) design (Fig. 19a) Ma and Su (2020); Ma et al. (2024). This design targets a narrow range of sound frequencies, with absorption dependent on the depth of the honeycomb core. A *Double Degree of Freedom* (DDOF) design (Fig. 19b) Ma and Su (2020); Ma et al. (2024), which incorporates two resonating layers, can be used to broaden the absorption bandwidth. However, this approach adds complexity and increases the weight of the structure.

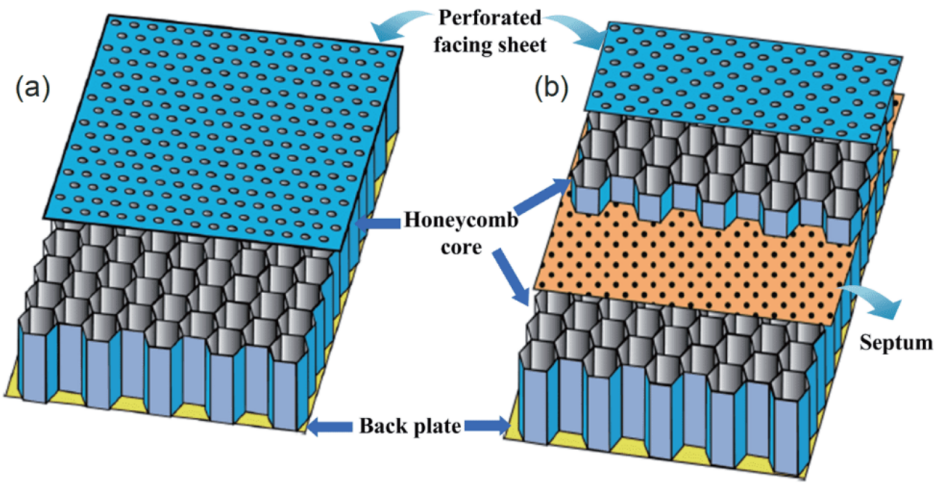


Figure 19: Liner basic structure Ma and Su (2020). (a) Single degree of freedom structure. (b) Double degree of freedom structure.

Those specific frequencies are tuned depending on the characteristics of the noise being targeted. Aircraft engines, for example, are usually designed to absorb low-frequency sounds generated by the fan and high-frequency noise from the combustion process Sugimoto et al. (2010). This tuning is critical because the effectiveness of the liner depends on the match between the sound frequencies and the resonator design.

3 ENODISE Results

The theoretical characteristics of several acoustic mitigation strategies have been discussed, namely the serrated trailing edge, flow and acoustic effects of porous media, and acoustic liners. As part of the ENODISE project, these acoustic mitigation strategies were then applied to the experimental configurations

3.1 Serrated Trailing Edge Propeller

As part of the ENODISE experimental campaign, the acoustic mitigation of serrated trailing edge propeller blades in the BLI condition was investigated. The blades were introduced to the Boundary Layer Ingestion experimental setup depicted in Figure 20. This consisted of a propeller rig placed adjacent to a curved plate upon which an adverse pressure gradient boundary layer was developed. The acoustic results were measured using two microphone arcs populated with GRAS 40PL microphones.

The curved section of the plate is defined by a cubic Bezier function with control points: Points $=[0, 0.2; 0.75, 0.2; 0.25, 0; 1, 0]$. The propeller rig is positioned 80 cm downstream of the nozzle exit. The flow is tripped with 80-grit sandpaper to initiate the development of a boundary layer which flows over the curved section of the plate, generating an adverse pressure gradient. The plate measures 1.69 m x 2 m and was made up of a thin plywood sheet formed over a CNC-cut plywood skeleton support structure which was in turn mounted on aluminium profiles. The trailing edge of the plate was lined with porous

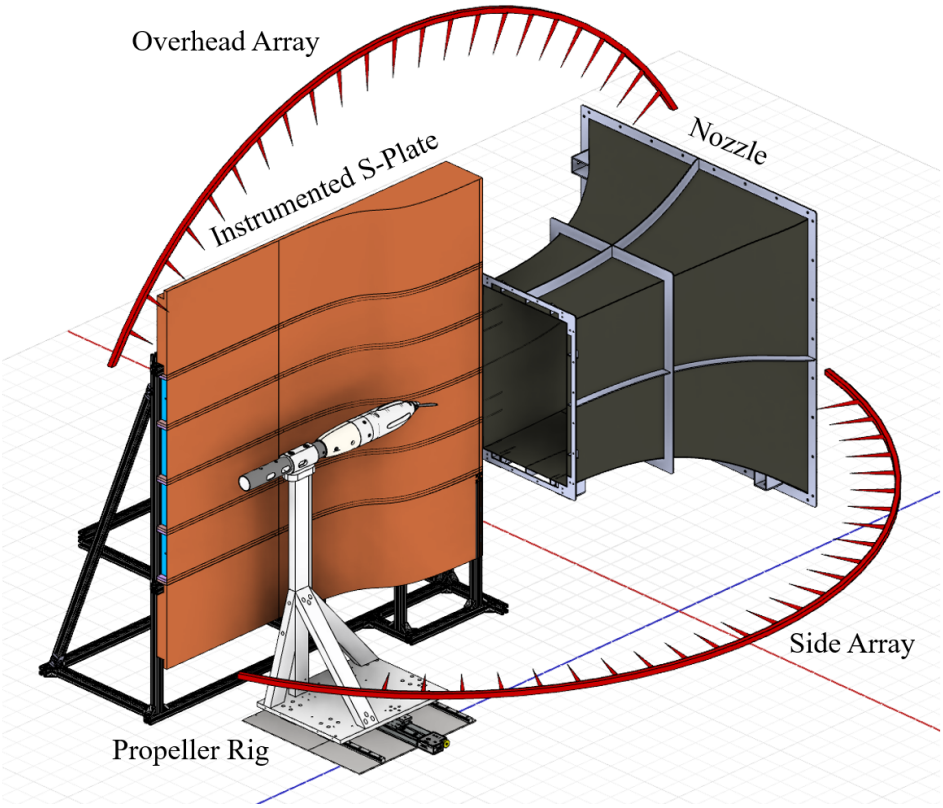


Figure 20: Schematic of the experimental configuration configuration

material to reduce trailing edge effects. The design of the propeller blade was modified to include trailing edge serrations, the blades were then 3D printed and tested. To design effective trailing-edge serrations for noise reduction, key parameters associated with the serrations were considered, namely the amplitude, h, and the wavelength, λ. According to Intravartolo et al., Intravartolo et al. (2017), the optimal ratio between the amplitude ($2h$) of the serrations and the mean aerodynamic chord was approximately 28%. Moreover, based on Howe's Howe (1991b,a) analytical model, it was also suggested that the wavelength-to-amplitude ratio (λ/h) should also be kept below 4. Thus, two sets of serrations were used, detailed in Table 1 and depicted in Fig. 21.

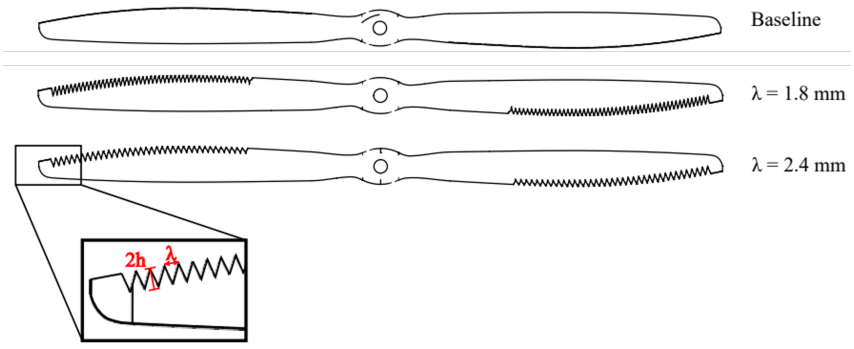


Figure 21: Geometry of the original and TE serrated blades with $\lambda/h = 0.9$ and 1.2.

Name	Amplitude, $2h$ (mm)	Wavelength, λ (mm)	λ/h
Fine	4	1.8	0.9
Coarse	4	2.4	1.2

Table 1: Description of the trailing edge serrations

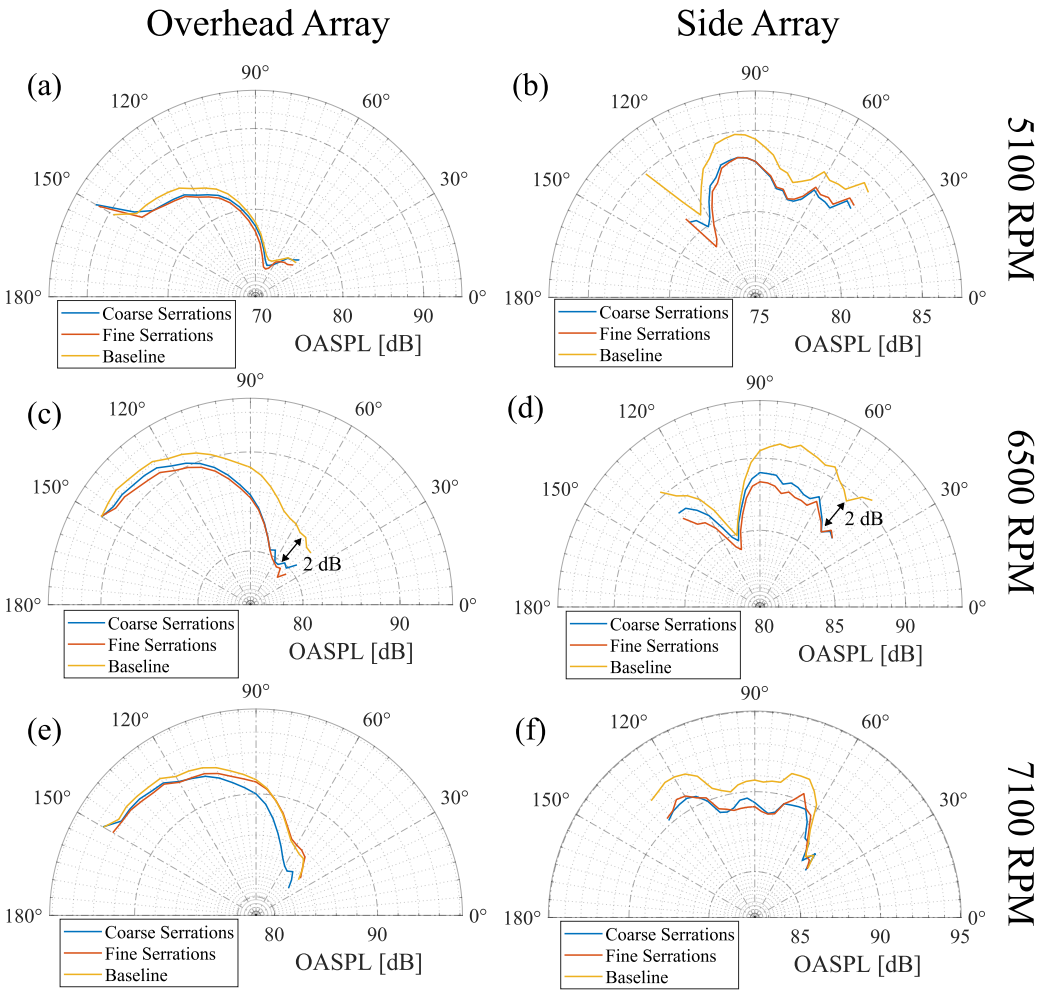


Figure 22: The OASPL directivity patterns for the blade TE serrations and comparison to the baseline case for both microphone arrays at three propeller speeds. Flow direction is from right to left.

Now let's take a look at the results of the application of trailing edge blade serrations on the far-field noise, with comparisons made to the baseline propeller (no serrations). Figure 22 presents the far-field directivity patterns of the serrated blades as measured by the overhead and side arrays, results for three propeller speeds (5100, 6500 and 7100 RPM) are shown as representing speeds that pertain to low, medium and high thrust conditions respectively. For the 5100 RPM case, Fig. 22a-b, the differences between the serrated blades and the baseline propeller are very minor across all polar angles in the overhead array while in the side array the baseline case present a consistent increase of approximately 1 dB over the serrations. The improvement in noise over the baseline case becomes more pronounced at the medium thrust case of 6500 RPM where now in the

overhead array, Fig. 22c, a reduction of 2 dB can be seen at upstream polar angles. This reduction is also clear in the side array, Fig. 22d, at similar upstream polar angles. However, increasing the RPM further to 7100 RPM reduces the effect of the serrations, the baseline still maintains the loudest noise emissions, but the differences are less clear, although now consistent across all side polar angles, Fig. 22f. Across all conditions, the OASPL differences between the coarse and fine serrations are negligible.

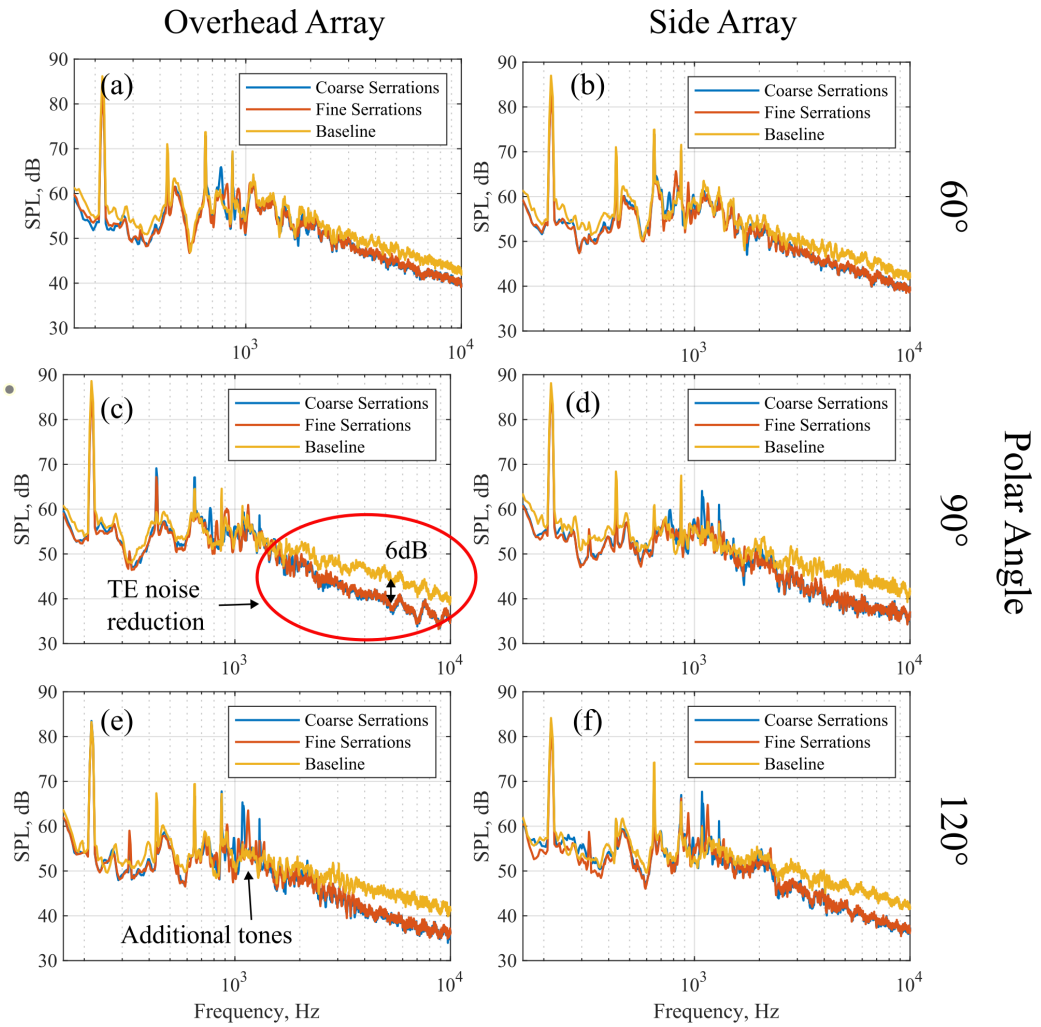


Figure 23: Far-field SPL spectra from three microphones in each polar arc presenting the results of the trailing edge serrations with comparisons to the baseline case for 6500 RPM.

The largest improvements of the serrated cases over the baseline propeller was observed at 6500 RPM, hence the SPL spectra are plotted for this case to determine the source of the noise reduction in OASPL. Figure 23 shows the SPL spectra of the serrated blades compared to the baseline case for polar angles of $60, 90$ and $120°$ in both the overhead and side arrays for 6500 RPM. Initial observations reveal consistent reduction in high frequency noise across all presented angles, in the order of 6 dB as seen in Fig. 23c. Trailing edge noise is predominantly present at these high frequency ranges and thus it can be seen that the serrations do contribute significantly to its reduction. The performance of the coarse and fine serrations in this frequency region are observed to be very similar with no notable

differences. However, it is noted, particularly at higher polar angles, that additional BPF harmonics are present for the serrated blades, which could explain the reduced overall noise reduction seen at these angles. Fine serrations are observed to present improved tonal performance as compared to the coarse serrations.

In summary, the trailing edge serrations on the blade noticeably reduced high-frequency noise at medium thrust conditions, at higher speeds the presence of additional tonal peaks caused the acoustic benefits to reduce. OASPL results show a clear reduction in noise at upstream angles only.

3.2 Acoustic Liners and Porous Materials

To investigate the absorption of sound waves from the propeller impacting the surface below, noise-mitigation materials were flush-mounted on the test section's bottom wall beneath the propeller, as shown in Fig. 24. Two types of materials were used for this mitigation strategy: quarter-wavelength resonator (QWR) arrays, functioning as band-stop noise absorbers, and a commercially available metal foam, which serves as a broadband noise absorber.

Each QWR array in this study was a rectangle with a total face area of 0.05×0.05 m^2. The arrays contained 49 tubes of varying lengths, each acting as an individual QWR. The tubes had radii of 2.75 mm, yielding a porosity of 47%. These arrays were designed to optimally absorb noise in the frequency range between 800 Hz and 1200 Hz.

A propeller and its propulsion system were placed downstream from the wind tunnel test-section inlet, near the bottom. The propeller clearance, i.e., the distance between the blade tips and the flat plate, was adjustable via a traverse system. A tripping device, consisting of a zigzag strip (8 mm height, 12 mm width, 60° angle), was installed 3.62 m upstream of the propeller plane to generate a turbulent boundary layer, which was crucial for understanding how turbulent-boundary-layer parameters affect the emitted noise. The propeller used was a two-bladed Meijzlik 12" × 18" (diameter 304.8 mm), with detailed geometric information available in Europa (2020). In contrast, information on the propulsion system and baseline noise characteristics is provided in Castelucci et al. (2023).

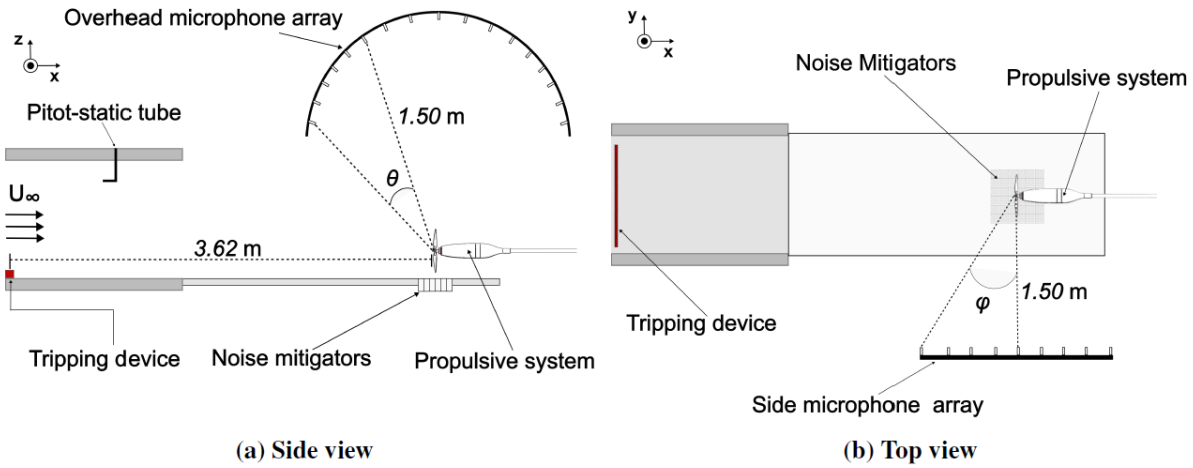


Figure 24: UTwente setup for the acoustic liners

Various spatial configurations of quarter-wave resonator (QWR) cells and flat reflective surfaces were tested to examine the impact of QWR-cell arrangements on the recorded noise levels and their directivity. These configurations involved distributing the QWR arrays across a 0.30×0.30 m^2 instrumentation surface beneath the propeller. Figure 25 illustrates the configurations, where white squares represent flat plates, perforated squares indicate QWR-cell units, and the propeller position is marked in red for reference.

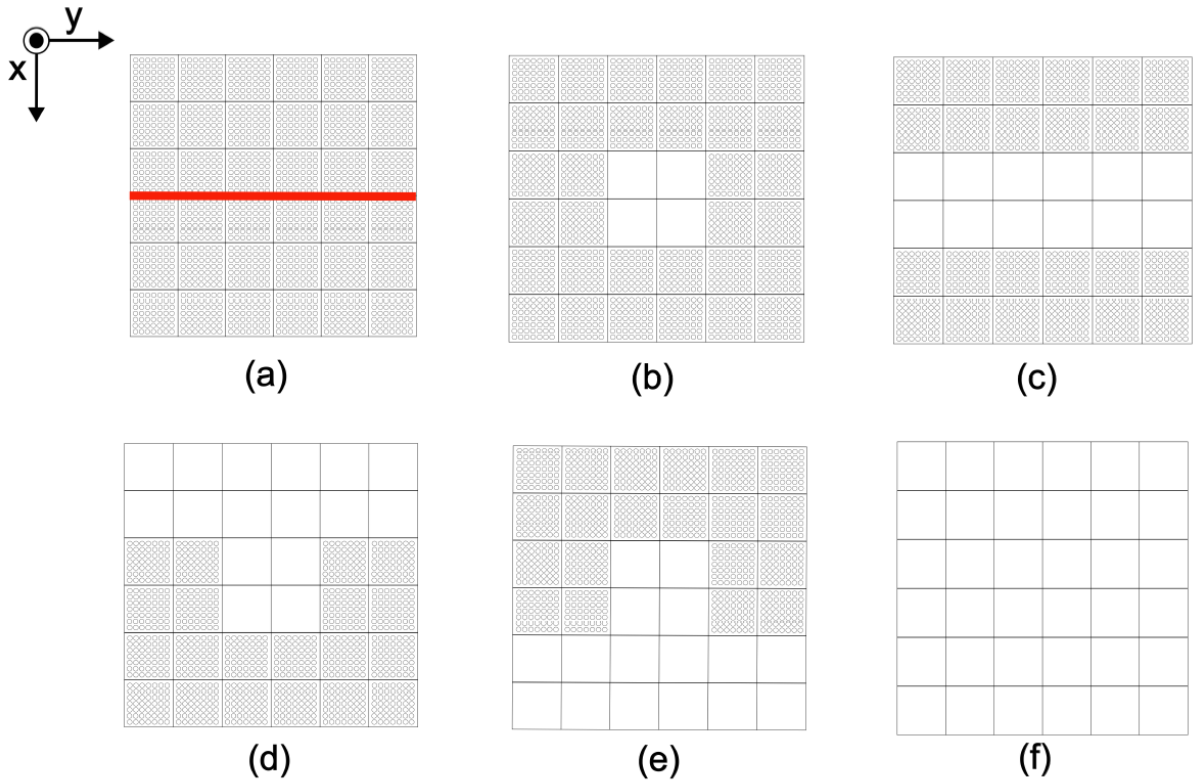


Figure 25: Distribution of the QWR beneath the propeller. The configurations will be referred to as follows: (a) Full-QWR. (b) Flat-plate-center. (c) Flat-plate-blade. (d) Downstream-only. (e) Upstream-only. (f) Full-flat-plate.

Figure 26 presents the recorded sound spectra from an overhead microphone at $\theta = 90°$, with a flow speed of U and the propeller rotating at 6000 RPM. The configurations tested include flat-plate-center (Fig. 26a), flat-plate-blade (Fig. 26b), downstream-only (Fig. 26c), and upstream-only (Fig. 26d). The results are compared to the full-flat-plate case (finely dotted grey line), where no QWR cells were applied, leaving the instrumentation plate as a hard surface. In Fig. 26a (flat-plate-center), the tonal increase is less significant than in the full-QWR configuration, though overall noise levels are higher than the no-QWR case (finely dotted black line). Fig. 26b shows that tonal peaks are mostly suppressed when the blade area is entirely covered with flat plates, except for the peak at 800 Hz. The downstream-only (Fig. 26c) and upstream-only (Fig. 26d) configurations exhibit increased tonal noise, particularly at the 4^{th} and 5^{th} blade passing frequencies (BPF). In cases where no QWR is installed beneath the rotating propeller, the effects observed in the full-QWR case are suppressed, confirming that the increased tonal peaks in the full-QWR configuration are due to a local hydrodynamic effect. These findings

indicate that the QWR cell directly beneath the propeller center contributes significantly to this effect.

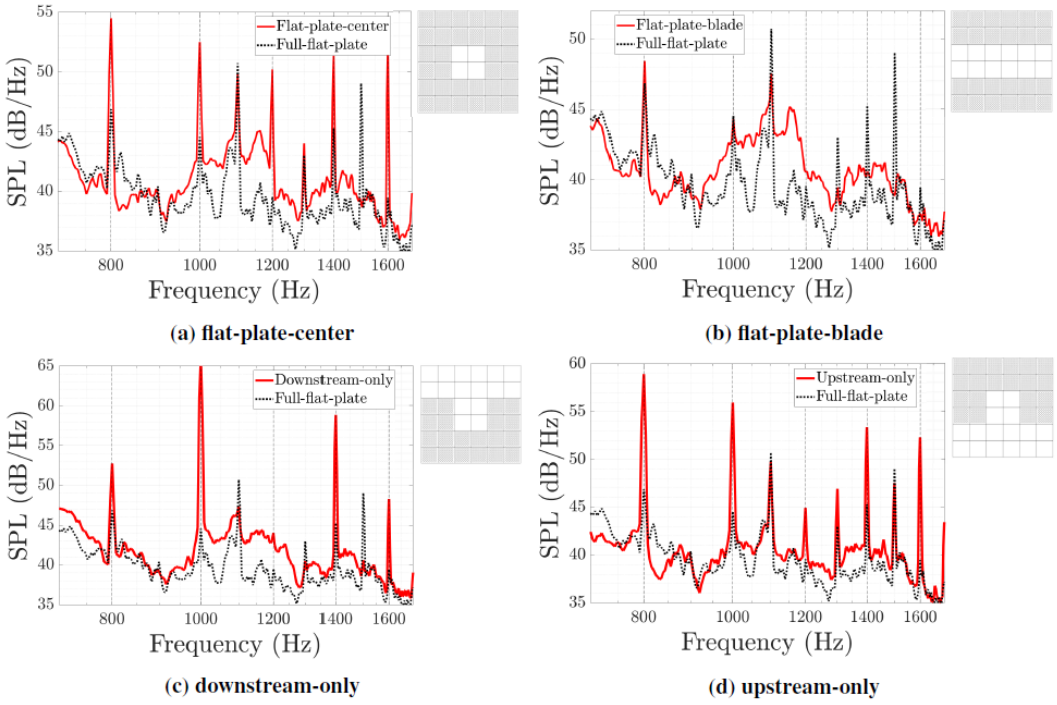


Figure 26: Noise spectra (zoom) of different QWR configurations. Forward speed $U_\infty = 30\ \mathrm{m \cdot s^{-1}}$, 6000 RPM, $\theta = 90°$ microphone and 5 mm clearance).

Based on the results above, the flat-plate-blade QWR-cell configuration was the most effective for reducing tonal peaks and overall noise. To assess the broader effectiveness of QWRs as a noise-mitigation strategy, this configuration was compared to a porous material, specifically metal foam, a standard noise absorber.

Figure 27 compares the recorded sound-pressure levels for the metal foam, flat-plate-blade QWR-cell configuration, and full-flat-plate reference. In the low-frequency range (1st and 2nd BPF), the metal foam showed higher tonal peaks, but in the mid-frequency range (4th to 8th BPF), it significantly reduced both tonal and broadband noise compared to the other configurations.

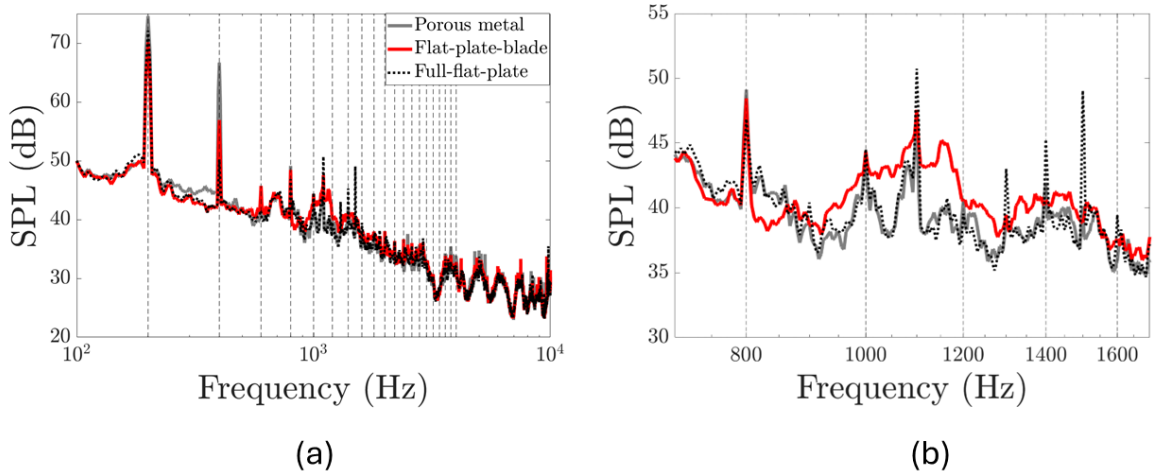


Figure 27: Noise spectra with optimal QWR and porous metal ($U_\infty = 30\ m \cdot s^{-1}$, 6000 RPM, $\theta = 90°$ microphone and 5 mm clearance).

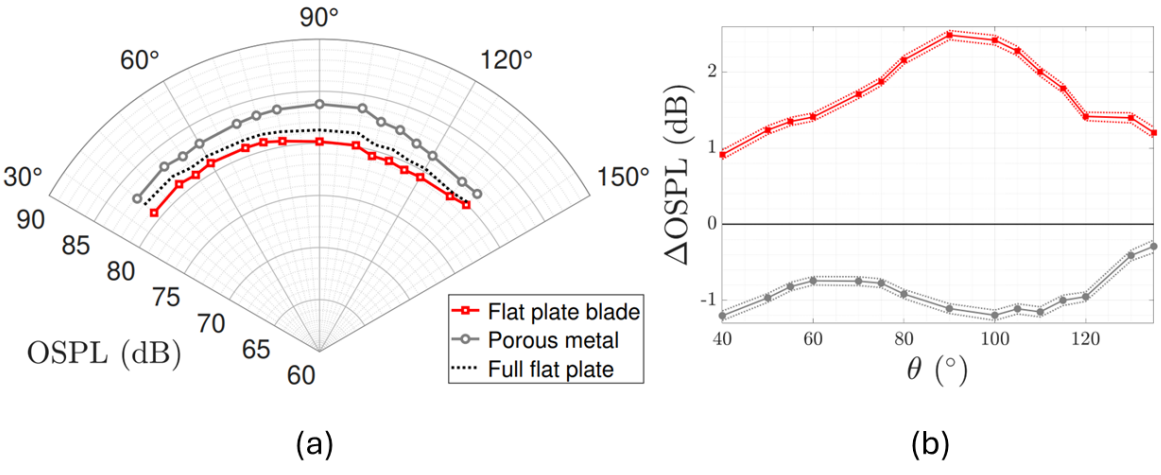


Figure 28: Overhead directivity for the QWR and porous metal mitigators ($U_\infty = 30\ m \cdot s^{-1}$, 6000 RPM and 5 mm clearance). (a) OSPL directivity. (b) Δ OSPL.

However, as shown in Fig. 28, in terms of overall sound pressure levels (OSPL), the metal foam caused an increase across the polar-angle range of 40° to 135°, with the

most pronounced effect between 80° and 100°. In contrast, the flat-plate-blade QWR configuration showed a general reduction in OSPL over the same angular range.

The side array experiment (Fig. 29) investigated the influence of QWR-cell configurations on azimuthal directivity by comparing two QWR setups (flat-plate-blade and downstream-only) and a porous metal foam. Results showed that all three noise-mitigation strategies caused an increase in OSPL between $\phi = 45°$and$\phi = 120°$ compared to the flat-plate reference, particularly in the upstream range (40° to 90°). However, this increase was less pronounced downstream, and beyond 120°, the results tended to align with the flat-plate reference. Among the strategies, the flat-plate-blade configuration showed the smallest increase in OSPL, making it the most effective of the configurations tested.

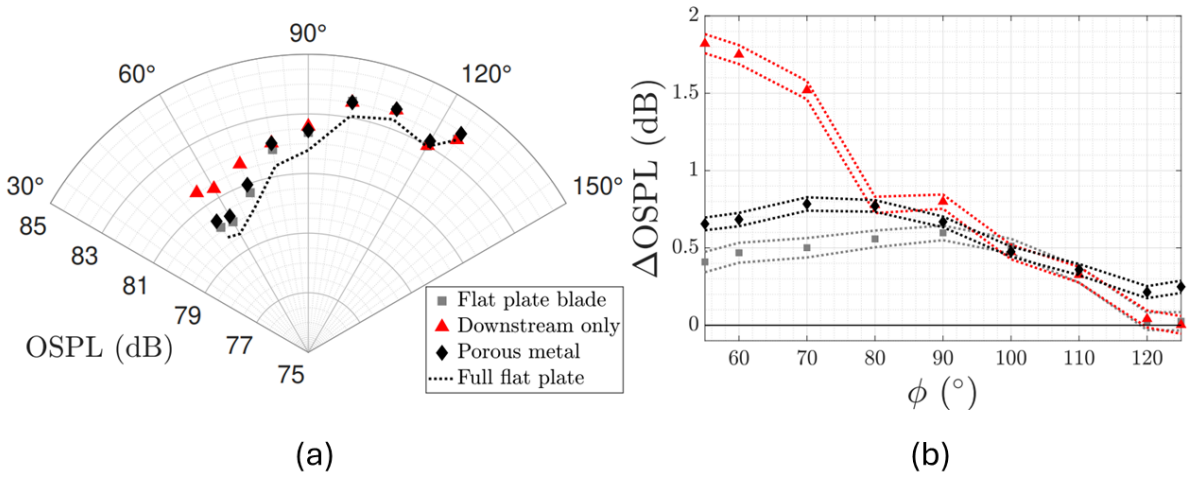


Figure 29: Side array directivity of different mitigators ($U_\infty = 30\ m \cdot s^{-1}$, 6000 RPM and 5 mm clearance). (a) OSPL directivity. (b) Δ OSPL.

4 Summary

Aeroacoustic installation effects, arising from the interaction between aerodynamic forces and noise generated by aircraft components, represent a significant challenge in modern aerospace engineering. These effects not only influence the performance of aircraft but also contribute to environmental noise pollution. The mitigation of such effects is critical to improving aircraft efficiency while meeting increasingly stringent noise regulations.

Here we explored some of the methods and techniques for mitigating aeroacoustic installation effects. Key strategies include the application of porous materials, serrated trailing edges, and acoustic liners, all of which are designed to balance both noise and aerodynamic performance.

Porous materials were shown to be highly effective in reducing noise generated by turbulent flow interactions. These materials alter boundary layer dynamics by allowing

airflow penetration, which disrupts turbulent structures, delays vortex shedding, and reduces pressure fluctuations. Experimental studies demonstrated the dual benefit of these materials, not only in noise mitigation but also in reducing aerodynamic drag, thus enhancing overall aircraft efficiency. Serrated trailing edges were another focus, specifically for their ability to reduce trailing-edge noise by scattering pressure waves from turbulent eddies. The serrations break up coherent turbulent structures, thereby diminishing noise emissions. Empirical investigations showed that the effectiveness of serrations is highly dependent on their geometric parameters, such as amplitude and wavelength, with optimized designs yielding up to 10 dB noise reductions. Acoustic liners, commonly used in propulsion systems, provide another layer of noise control by absorbing sound waves and preventing their propagation. By using perforated face sheets over honeycomb cores, liners function as Helmholtz resonators, targeting specific noise frequencies generated by engines. We reviewed both single and double degree-of-freedom liner configurations, emphasizing the balance between noise absorption and maintaining aerodynamic efficiency.

As part of the ENODISE project, these mitigation strategies were applied to the boundary layer ingestion configurations to evaluate their applicable benefits. Tests involving trailing-edge serrations on propeller blades demonstrated reductions in high-frequency noise, particularly under medium thrust conditions. Additionally, the use of porous materials and acoustic liners beneath propellers showed significant promise in reducing both tonal and broadband noise.

Overall, we underscore the importance of integrating noise mitigation technologies into aircraft design. By addressing both aerodynamic performance and noise control, these technologies contribute to the development of quieter, more efficient, and environmentally friendly aircraft. The application of advanced materials and configurations, combined with ongoing empirical research, will continue to drive progress in mitigating adverse aeroacoustic installation effects, shaping the future of sustainable aviation.

References

Ali, S. A. S., Azarpeyvand, M., and Silva, C. R. I. D. (2018a). Trailing-edge flow and noise control using porous treatments. *Journal of Fluid Mechanics*, 850:83–119.

Ali, S. A. S., Azarpeyvand, M., Szoke, M., and Silva, C. R. I. D. (2018b). Boundary layer flow interaction with a permeable wall. *Physics of Fluids*, 30.

Bauer, A. B. (1977). Impedance theory and measurements on porous acoustic liners. *Journal of Aircraft*, 14(8):720–728.

Castelucci, L. A., Venner, C. H., and de Santana, L. D. (2023). Experimental analysis of the noise of small propellers subjected to non-uniform inflow. In *AIAA SCITECH 2023 Forum*, page 1545.

Europa, C. (2020). Development of computational and experimental noise assessment and suppression methodologies for the next generation of silent distributed propulsion configurations. Last accessed 30 May 2022.

Galles, M. B., Jones, M. G., and Nark, D. M. (2022). An initial assessment of variable depth liner optimization for ducted proprotor applications. In *28th AIAA/CEAS Aeroacoustics 2022 Conference*, page 2821.

Howe, M. S. (1991a). Aerodynamic noise of a serrated trailing edge. *Journal of Fluids and Structures*, 5(1):33–45.

Howe, M. S. (1991b). Noise produced by a sawtooth trailing edge. *Journal of the Acoustical Society of America*, 90(1):482–487.

Howerton, B. M. and Jones, M. G. (2018). Acoustic liner drag: further measurements on novel facesheet perforate geometries. In *2018 AIAA/CEAS Aeroacoustics Conference*, page 3605.

Intravartolo, N., Sorrells, T., Ashkharian, N., and Kim, R. (2017). Attenuation of vortex noise generated by UAV propellers at low Reynolds numbers. In *AIAA SciTech Forum - 55th AIAA Aerospace Sciences Meeting*, pages 1–11.

Jones, M. G., Simon, F., and Roncen, R. (2022). Broadband and low-frequency acoustic liner investigations at nasa and onera. *AIAA Journal*, 60(4):2481–2500.

Lilley, G. (2004). A quest for quiet commercial passenger transport aircraft for take-off and landing. In *10th AIAA/CEAS Aeroacoustics Conference*, page 2922.

Lyu, B., Azarpeyvand, M., and Sinayoko, S. (2016). Prediction of noise from serrated trailing edges. *Journal of Fluid Mechanics*, 793:556–588.

Ma, P., Wang, H., Li, D., Yuan, S., and Fan, X. (2024). Passive acoustic liners for aero-engine noise control: A review. *Mechanics of Advanced Materials and Structures*, pages 1–16.

Ma, X. and Su, Z. (2020). Development of acoustic liner in aero engine: a review. *Science China Technological Sciences*, 63:2491–2504.

Sirotto, J. R., Bonomo, L. A., and Cordioli, J. A. (2024). On the application of acoustic liners for the reduction of jet-flap installation noise. *Applied Acoustics*, 221:110029.

Sugimoto, R., Astley, R. J., and Murray, P. B. (2010). Low frequency liners for turbofan engines. In *Proceedings of the 20th International Congress on Acoustics*, page 4. Australian Acoustical Soc. Sydney, Australia. `https://www.acoustics.asn.au/conference_proceedings/ICA2010/cdrom-ICA2010/papers/p575.pdf`.

Tang, P. and Sirignano, W. (1973). Theory of a generalized helmholtz resonator. *Journal of Sound and Vibration*, 26(2):247–262.